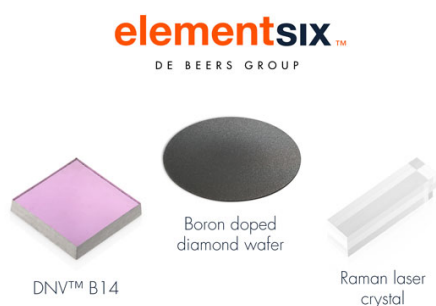


OPEN ACCESS

Pt-Catalyzed Oxidation of PEMFC Carbon Supports: A Path to Highly Accessible Carbon Morphologies and Implications for Start-Up/Shut-Down Degradation

To cite this article: Timon Lazaridis and Hubert A. Gasteiger 2021 *J. Electrochem. Soc.* **168** 114517

View the [article online](#) for updates and enhancements.



Element Six is a world leader in the development and production of synthetic diamond solutions

Since 1959, our focus has been on engineering the properties of synthetic diamond to unlock innovative applications, such as thermal management, water treatment, optics, quantum and sensing. Our patented technology places us at the forefront of synthetic diamond innovation, enabling us to deliver competitive advantage to our customers through diamond-enabled solutions.

Find out more and contact the team at:
ustechnologies@e6.com





Pt-Catalyzed Oxidation of PEMFC Carbon Supports: A Path to Highly Accessible Carbon Morphologies and Implications for Start-Up/Shut-Down Degradation

Timon Lazaridis^{*,z}  and Hubert A. Gasteiger^{**} 

Chair of Technical Electrochemistry, Department of Chemistry and Catalysis Research Center, Technical University of Munich, D-85748 Garching, Germany

The morphology of carbon supports for Pt-based proton-exchange membrane fuel cell (PEMFC) catalysts strongly determines their performance at both low and high current density. Porous carbon supports with internally deposited Pt nanoparticles sustain high kinetic activity by shielding Pt from ionomer adsorption, albeit at the expense of poor oxygen mass transport. This work systematically explores an oxidative pre-treatment of commercial Pt/Ketjenblack, termed *localized oxidation*, which drastically improves oxygen transport and high current density performance (up to 50% at 0.6 V). The method leverages Pt-catalyzed carbon oxidation in the immediate vicinity of internal Pt particles to increase pore accessibility. We analyze the catalyst morphology *via* N₂ physisorption and thermogravimetric analysis (TGA), and correlate these results with extensive electrochemical characterization of low-loaded cathodes (0.06 mg_{Pt} cm⁻²). High current density gains are shown to result predominantly from removing microporous constrictions in the primary carbon particle. We further identify a trade-off between Pt particle sintering and pore widening dependent on the oxidation temperature, which defines an optimum degree of oxidation. Finally, we investigate the susceptibility of locally oxidized catalysts towards start-up/shut-down (SUSD) degradation. Although we find modestly accelerated degradation rates at high oxidation temperatures, this does not outweigh the performance benefit imparted by the pre-treatment. © 2021 The Author(s). Published on behalf of The Electrochemical Society by IOP Publishing Limited. This is an open access article distributed under the terms of the Creative Commons Attribution 4.0 License (CC BY, <http://creativecommons.org/licenses/by/4.0/>), which permits unrestricted reuse of the work in any medium, provided the original work is properly cited. [DOI: 10.1149/1945-7111/ac35ff]



Manuscript submitted August 9, 2021; revised manuscript received October 13, 2021. Published November 26, 2021.

Global interest in PEM fuel cells for emission-free transport and mobility continues to surge, particularly in applications which are not easily electrifiable with Li-ion batteries, e.g. heavy-duty vehicles and maritime vessels.¹ Large-scale commercialization, however, hinges on cost-competitiveness with incumbent technologies.² Increasing Pt efficiency by reducing Pt content or maximizing high current density performance thus is particularly important in high-volume production scenarios, because raw materials such as Pt constitute cost factors which generally do not benefit from economies of scale.^{3–5} In recent years, researchers have stressed the central role of the carbon support in enabling high catalyst performance at low Pt loadings.⁶ Commonly used catalysts consist of Pt or Pt-alloy nanoparticles dispersed onto carbon blacks, the primary particles of which can have widely different morphologies. In this context, a useful classification can be made by distinguishing whether carbons are structurally capable of hosting 2–4 nm Pt nanoparticles in an internal porous network. Solid carbons may be non-porous (graphitized carbons) or microporous (Vulcan), but crucially cannot accommodate Pt nanoparticles internally. As a consequence, all Pt nanoparticles must be present on the primary carbon particle's external surface.⁷ In contrast, porous carbons (or high surface area carbons, HSCs) display large internal mesoporosity. Commonly used deposition by impregnation yields a large fraction of Pt nanoparticles located inside the primary carbon particles; for the most prominent HSC, Ketjenblack, the fraction of internal Pt particles in commercially available catalysts amounts to 60%–70%.⁸

Both carbon morphologies have characteristic impacts on catalyst performance. Since Pt nanoparticles are predominantly present on the external surface of solid carbons, they are necessarily in intimate contact with the ionomer film percolating through the electrode. It thus becomes possible for sulfonate end groups at the end of the ionomer side-chains to adsorb onto the Pt surface. While the adsorption strength may vary based on ionomer structure, electrode potential, and relative humidity, it inevitably affects the oxygen reduction reaction (ORR) kinetics negatively by competitive blocking of oxygen adsorption sites.^{9,10} This *ionomer poisoning* results in depressed mass activities and lower cell voltages at low

current density for solid carbons. On the other hand, external Pt particles on solid carbons are perfectly accessible to diffusing O₂ and therefore perform well at high current densities, where the cell voltage is primarily governed by mass-transport limitations and flooding effects. These two phenomena reverse in porous carbons. Due to size exclusion, ionomer chains cannot adsorb onto Pt particles that are mostly present in the internal pores, resulting in 2–4 times higher ORR mass activities.¹¹ At high current densities, however, the necessity for O₂ to pass through constricted pores to reach the Pt nanoparticles located inside the carbon primary particles increases the oxygen mass transport resistance, aggravating the associated voltage loss.^{8,12} In essence, one faces a trade-off between ORR activity and oxygen transport depending on the location of the Pt nanoparticles on/inside the support. A widely regarded publication by Yarlagadda et al. pointed out this dilemma and presented the concept of a carbon support with an intermediate support morphology, which they termed “accessible porous carbon.”¹³ This material was suggested to feature an internal pore structure in which Pt nanoparticles would be shielded from ionomer contact to allow for high ORR activity, while the pore geometry would be tailored such as to not incur oxygen transport-related losses. Although the provenance of such supports is not revealed, performance data indicate that their material succeeded in uniting high mass activity and low oxygen transport losses.

In this context it is interesting to note that General Motors has filed patent applications on a post-treatment of Pt/HSC catalysts, making use of the precious metal's catalytic activity for carbon oxidation.^{14,15} In the presence of air and at adequately controlled temperatures, oxidative removal of carbon as CO₂ can be restricted to occur only in the immediate vicinity of Pt nanoparticles, so that the pores in the carbon support in the vicinity of the internally located Pt nanoparticles essentially open up, thereby enabling better oxygen mass transport while retaining the protection of Pt nanoparticles from sulfonate adsorption. As demonstrated by the disclosed polarization curves, this process is well-suited to obtain the above discussed “accessible porous carbon” morphology. One might thus speculate that the catalyst materials presented in Yarlagadda et al.'s original account and in subsequent General Motors-affiliated publications were produced in a similar fashion.^{16,17} These works, however, never detail the origin of the used carbon supports and whether they were prepared prior to the deposition of Pt

*Electrochemical Society Student Member.

**Electrochemical Society Fellow.

^zE-mail: timon.lazaridis@tum.de

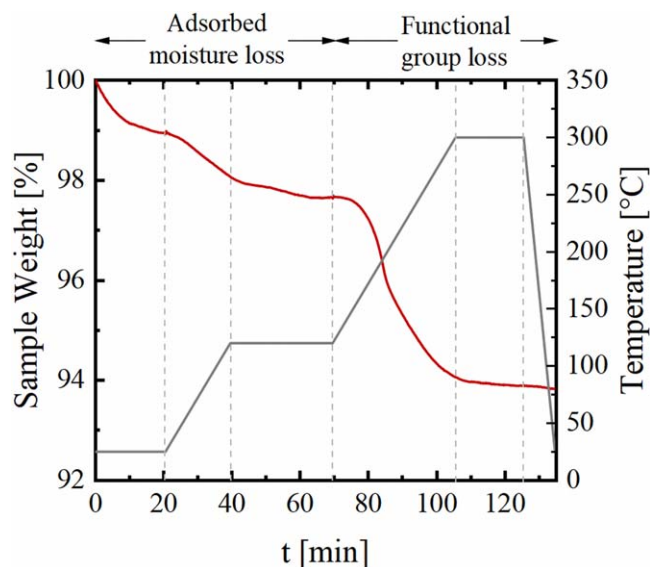


Figure 1. Mass loss of the pristine Pt/KB catalyst stored under ambient atmosphere upon heating under oxygen-free atmosphere, determined by thermogravimetric analysis under an Ar flow (red, plotted on the left-hand y-axis); the temperature ramps (black, plotted on the right-hand y-axis) are at 5 K min⁻¹. The mass loss by the end of the 120 °C hold corresponds to the desorption of moisture, while the mass loss above 120 °C is attributed to the loss of functional groups on the carbon surface.

nanoparticles or whether they were produced by the oxidation of Pt/HSC catalysts, and so no detailed study of the localized oxidation of carbon supports can be found in the academic literature to date. Another closely related question would be whether localized carbon oxidation increases the catalyst's susceptibility towards start-up/shut-down (SUSD) degradation, a major failure mode for long-term cell operation. During SUSD events, H₂/air fronts traversing the anode compartment induce reversed currents through the membrane in the air-filled portion of the anode flow-field, leading to the oxidation of the carbon support of the platinum catalyst in the adjacent cathode electrode.¹⁸ Ultimately, this electrochemical oxidation of the carbon support leads to a collapse of the cathode electrode's microstructure and a concomitant stark decrease in cell performance due to an impeded oxygen mass transport.^{19,20} It is conceivable that the carbon loss during the above described localized carbon oxidation of at Pt/HSC catalyst also accelerates SUSD degradation, which would limit the practical applicability of such catalysts.

In the present work, we investigate the localized carbon oxidation of commercial Ketjenblack supported Pt catalyst (Pt/KB) by subjecting it to heat treatments ranging from 230 °C to 290 °C in an air/Ar mixture. In this manner, the degree of localized carbon oxidation can be incrementally controlled up to a threshold temperature, and morphological changes imparted by the treatment are assessed using N₂ physisorption and thermogravimetric analysis. Electrochemical characterization of both pristine and pre-oxidized Pt/KB catalysts is carried out in 5 cm² single-cells and correlated to the changes in the carbon support structure. H₂/O₂ and H₂/air polarization curves are supported by quantification of the proton conduction resistance via electrochemical impedance spectroscopy (EIS) and of the oxygen transport resistance from limiting current measurements in order to allow for a comprehensive voltage loss analysis. In addition, the impact of localized oxidation on SUSD degradation susceptibility is explored in a 50 cm² cell setup.

Experimental

Oxidative heat treatment of Pt/Ketjenblack catalyst.—300 mg of as-received commercially available 18.8 wt% Pt/Ketjenblack (Pt/KB; TEC10E20E, Tanaka Kikinokoku K.K., Japan) was placed in an

alumina crucible and transferred to a tube furnace (Carbolite Gero GmbH & Co KG, Germany). After flushing with Ar gas, a temperature ramp (10 K min⁻¹) was set to a target oxidation temperature (230 °C–290 °C). Upon reaching the desired temperature, the gas flow was switched to a mixture of synthetic air (1000 ml min⁻¹) and argon (200 ml min⁻¹), and held for 12 h. The sample was then left to cool down to room temperature under argon flow. The mass loss was measured by weighing the catalyst powder immediately after opening the tube furnace in order to minimize reuptake of atmospheric moisture.

Microstructure of the Pt/KB catalyst.—Pore volumes and pore size distributions of pristine and oxidized Pt/KB powders were evaluated by N₂ physisorption at 77 K using an Autosorb iQ gas sorption analyzer (Quantachrome Instruments, USA). All samples were evacuated at 100 °C for 18 h prior to physisorption experiments. Adsorption and desorption of all samples were recorded in the relative pressure range of 10⁻⁵ > p/p₀ > 0.995, where *p* represents the gas pressure and *p*₀ the saturation pressure of N₂. Specific surface area, pore volume, and the pore size distribution were calculated using a quenched solid density functional theory (QSDFT) kernel for slit/cylindrical pores (embedded in the ASiQwin software). In order to avoid artefacts stemming from the forced closure of the hysteresis at p/p₀ = 0.42, the QSDFT method was applied to the adsorption branch. Evaluating N₂ physisorption isotherms via QSDFT rather than the Barrett–Joyner–Halenda (BJH) method is based on the observation that the latter methods do not sufficiently account for carbon heterogeneity and therefore tend to produce larger errors when estimating pore volumes and pore size distributions in materials with microporosity.²¹

Determination of the carbon loss upon Pt/KB oxidation.—For an initial evaluation of the extent of carbon oxidation vs temperature under the above given air/Ar mixture, the oxidation of the pristine catalyst was evaluated by thermogravimetric (TGA) measurements. For this, 10 mg of the pristine Pt/KB catalyst were placed in a 150 μl sapphire crucible and heated under Ar flow (120 nccm) to a given target temperature (250 °C, 300 °C, and 350 °C) at 10 K min⁻¹. Once the target temperature was reached, an additional air flow was added (100 nccm) while the Ar flow was reduced to 20 nccm and the mass loss was measured over 12 h, mimicking the above described heat treatment procedure in the tube furnace. The total mass loss of the Pt/KB catalysts oxidized in TGA was then compared to that obtained in the tube furnace (see above).

In order to understand the structural changes caused by the oxidation process, one needs to quantify the mass loss contributions of adsorbed water, carbon surface functionalities, and carbon lost from the pore structure itself (i.e., the bulk carbon loss). As water and functional groups may also be removed by heating in an inert gas, their contributions can be estimated by thermogravimetric analysis of the pristine Pt/KB powder under an argon flow (120 nccm). Heating to 120 °C at 5 K min⁻¹ with a 25-min hold removes adsorbed moisture, subsequent heating to 300 °C at 5 K min⁻¹ with a 15-min hold then marks the desorption of functional groups. The mass loss in this experiment for pristine Pt/KB stored under ambient conditions is shown in Fig. 1, indicating a mass loss of ~2.3 wt% due to adsorbed water and of ~3.8 wt% due to the desorption of functional groups. From this measurement, the bulk carbon loss can be estimated by subtracting the total mass loss under argon from the total mass loss obtained by heating to the same temperature under an air/argon mixture flow in the tube furnace (see above).

Determination of Pt loading.—The Pt content of pristine and oxidized Pt/KB catalysts was independently determined via thermogravimetric analysis (TGA) and atomic adsorption spectroscopy (AAS). In TGA (Mettler Toledo, Switzerland) measurements, the catalyst was heated in pure O₂ gas at a temperature ramp of 10 K min⁻¹ to 700 °C in order to completely combust the carbon. The residual mass was taken as the Pt content. AAS was carried out in an

AA280 FS spectrometer (Agilent, USA). Both methods were in excellent agreement for the pristine Pt/KB (18.8 wt%), but deviated slightly with increasing oxidation temperatures (up to 1 wt%). As literature reports on the formation of gaseous PtO_x at high temperatures ($>600\text{ }^\circ\text{C}$),²² the Pt loading was exclusively taken from AAS to avoid underestimations.

Membrane electrode assembly (MEA) preparation.—MEAs with an active area of 5 cm^2 were prepared by the decal transfer method. Catalyst inks were prepared by mixing the pristine or oxidized Pt/KB catalyst powder, ultrapure water (MilliQ Millipore), 1-propanol (HPLC grade), and the ionomer dispersion (Asahi Kasei, Japan, 735 EW) in an 8 ml HDPE bottle containing 5 mm ZrO_2 beads. The carbon content of the dispersion was adjusted from 22–24 $\text{mg}_{\text{Carbon}}\text{ ml}^{-1}$, while the water content was fixed at 10 wt%. The ionomer-to-carbon mass ratio (I/C) was set to 0.65. Anodes were prepared by the same procedure from commercial 20.0 wt% Pt/Vulcan catalyst (TEC10V20E, TKK), albeit at a higher carbon content of 30 $\text{mg}_{\text{Carbon}}\text{ ml}^{-1}$. All catalyst inks were mixed on a roller mill (80 rpm) for 18 h at room temperature and subsequently coated onto virgin PTFE using a Mayer rod coater. The MEAs were prepared by hot-pressing anode/cathode decals at $155\text{ }^\circ\text{C}$ for 3 min onto a $15\text{ }\mu\text{m}$ reinforced membrane (low EW, non-mitigated GORE-SELECT[®], W.L. Gore and Associates). Noble metal loadings were determined by weighing decals before and after hot-pressing. The thus obtained cathode Pt loadings for the MEAs with the pristine and oxidized Pt/KB catalysts were all within $0.062 \pm 0.004\text{ mg}_{\text{Pt}}\text{ cm}^{-2}$ (see Table III) and $0.100 \pm 0.015\text{ mg}_{\text{Pt}}\text{ cm}^{-2}$ for the anodes. To compare the oxygen mass transport properties of the highly porous Ketjenblack-based catalysts with that of a less porous carbon support for which most of the Pt nanoparticles are located on the external carbon surfaces, MEAs with pristine Vulcan-carbon supported platinum (20 wt% Pt/Vu; TEC10V20E, Tanaka Kikinzoku K.K., Japan) with a similar Pt loading were prepared (see Table III).

MEAs with an active area of 50 cm^2 were prepared in an identical fashion as described above, except that the cathode loadings were increased to $0.10 \pm 0.004\text{ mg}_{\text{Pt}}\text{ cm}^{-2}$ and that a mitigated $15\text{ }\mu\text{m}$ reinforced membrane was used (low EW, mitigated GORE-SELECT[®] Membrane from W. L. Gore and Associates).

For thickness determination, square cut-outs of pristine MEAs with approximately 0.5 mm edge length were fixated on adhesive Cu tape. Clean cross-sections of these composites were prepared in an IB-19520 cooling cross-section polisher (JEOL Ltd., Japan) at $-95\text{ }^\circ\text{C}$, using a 3 h rough polishing step (6.0 kV, 10/10 s on/off) followed by a 1 h fine polish (4.0 kV, 5/10 s on/off). SEM micrographs of the polished cross-sections were taken on a FE-SEM JSM-7500F (JEOL Ltd., Japan) at 1 kV acceleration voltage and a working distance of 8.0 mm. Further details are given in the Appendix and the thicknesses of the MEAs with the pristine and differently pre-treated Pt/KB catalysts are given in Table III.

Testing hardware and MEA conditioning.—Fuel cell measurements were carried out in a stainless steel single-cell hardware (Fuel Cell Technologies, USA) fitted with 5 cm^2 active area graphite flow fields (0.5 mm wide channels and lands, Poco Graphite). For anode and cathode, Freudenberg H14C7 was used as a diffusion medium with a compression of 20%, which was set by using incompressible fiber-glass PTFE sub-gaskets to backstop an assembling torque of 12 Nm. Testing was performed on an automated Greenlight G60 test station. All MEAs were conditioned before full characterization using a voltage-controlled break-in procedure (H_2/air at 1390/3320 nccm, $80\text{ }^\circ\text{C}$, 100% relative humidity (RH), and 150 $\text{kPa}_{\text{abs,inlet}}$), following a sequence of 0.6 V (45 min), open circuit voltage (5 min) and 0.85 V (10 min) for 10 cycles. After the conditioning procedure, reversible losses were recovered by holding the MEA at 0.3 V for 2 h under H_2/air (2000/5000 nccm) at $40\text{ }^\circ\text{C}$, 270 $\text{kPa}_{\text{abs,inlet}}$, and 100% RH.

For start-up/shut-down experiments, a stainless steel single-cell hardware (Fuel Cell Technologies) was fitted with 50 cm^2 active area graphite flow fields (0.5 mm wide channels and lands, Poco Graphite). Both anode and cathode used Freudenberg H14C10 as a diffusion medium. Testing was performed on an automated Greenlight G60 test station. All MEAs were conditioned before full characterization using a voltage-controlled break-in procedure (H_2/air at 1390/3320 nccm, $80\text{ }^\circ\text{C}$, 100% relative humidity (RH), and 150 $\text{kPa}_{\text{abs,inlet}}$), following a sequence of 0.6 V (45 min), open circuit voltage (5 min) and 0.85 V (10 min) for 8 cycles. No recovery protocol was implemented in this case.

Fuel cell diagnostics with 5 cm^2 active area cells.—The electrochemically accessible surface area (ECSA) was determined via cyclic voltammograms (CVs) recorded on the cathode electrode between 0.07 and 0.6 V (150 mV s^{-1} scan rate, $40\text{ }^\circ\text{C}$, 110 $\text{kPa}_{\text{abs,inlet}}$) either after 30 cleaning cycles between 0.015 and 0.945 V at 100 mV s^{-1} at the beginning-of-life or directly after the intermittent recovery cycles. The counter/reference electrode was fed with 1000 nccm fully humidified 5% H_2/N_2 , while the cathode flow was set to 50 nccm of dry N_2 . The ECSA was then calculated by averaging the integrated H-adsorption and -desorption charges with a specific charge of $210\text{ }\mu\text{C cm}^{-2}_{\text{Pt}}$.

The proton conduction resistance in the cathode ($R_{\text{H}^+, \text{cath}}$) was determined from AC impedance spectra recorded in H_2/N_2 (anode/cathode) at 0.2 V_{cell} with a peak-to-peak perturbation of 3.5 mV between 500 kHz and 0.2 Hz (20 points per decade). Proton conduction resistances were measured at relative humidities of 100% and 70% RH, with cell pressures adjusted to 270 and 255 $\text{kPa}_{\text{abs,inlet}}$ to maintain identical H_2 and N_2 partial pressures for all experiments. Differential flow conditions for H_2/N_2 (1000/1000 nccm) were used at $80\text{ }^\circ\text{C}$. The proton conduction resistivity ($\rho_{\text{H}^+, \text{cath}}$) was calculated by dividing $R_{\text{H}^+, \text{cath}}$ by the cathode electrode thickness determined from SEM cross-sectional analysis (see above).

Differential flow polarization curves were recorded in current-controlled mode at $80\text{ }^\circ\text{C}$, 170 $\text{kPa}_{\text{abs,inlet}}$, 100% RH for both reactants, and constant flow of 2000 nccm of H_2 on the anode and 5000 nccm of O_2 or air on the cathode. Anode and cathode were operated in counter-flow mode. At these conditions, the pressure drop between inlet and outlet for anode and cathode was 2 and 22 kPa_{abs} , respectively. Prior to recording a polarization curve, the cathode potential was held at 0.75 V for 15 min. Current density points were then recorded from low to high current density, with the exception of the open circuit voltage point that was recorded last. Each measurement point was held for 10 min and the cell voltage was averaged over the final 30 seconds. The ORR kinetics (mass activity, i_m , and Tafel slopes) were determined from H_2/O_2 polarization curves after applying two corrections: i) the potential was corrected for the iR -drop, using the high frequency resistance (R_{HFR}) obtained from the x -axis intersect in the Nyquist plot measured by galvanic electrochemical impedance spectroscopy (GEIS) in the frequency range from 100 kHz to 10 Hz at each current density point (applying a 10% AC amplitude with the respect to the current); ii) the current was corrected for the shorting current of the membrane (i_{short} , calculated from the measured shorting resistance in the range of $R_{\text{short}} = 2\text{--}10 \cdot 10^3\text{ }\Omega\text{ cm}^2$), as well as for the H_2 crossover ($i_{\text{H}_2-x} = 5.5 \pm 0.5\text{ mA cm}^{-2}$), both determined in H_2 (anode, 600 nccm) and N_2 (cathode, 150 nccm) at 170 $\text{kPa}_{\text{abs,inlet}}$, $80\text{ }^\circ\text{C}$, and 100% RH by applying a constant potential of 0.3, 0.4, 0.5, 0.6 and 0.7 V for 2 min each.

The total mass transport resistance ($R_{\text{O}_2}^{\text{total}}$) was extracted from oxygen limiting current measurements at $80\text{ }^\circ\text{C}$ and 70% RH under differential flow conditions (2000 nccm of H_2 and 5000 nccm of O_2/N_2 mixtures). The dry mole fraction of oxygen was altered from 0.5 to 28% O_2 (rest N_2), while the cell potential was set to 0.30, 0.15, 0.10, and 0.05 V for 2 min each. To quantify pressure-dependent and

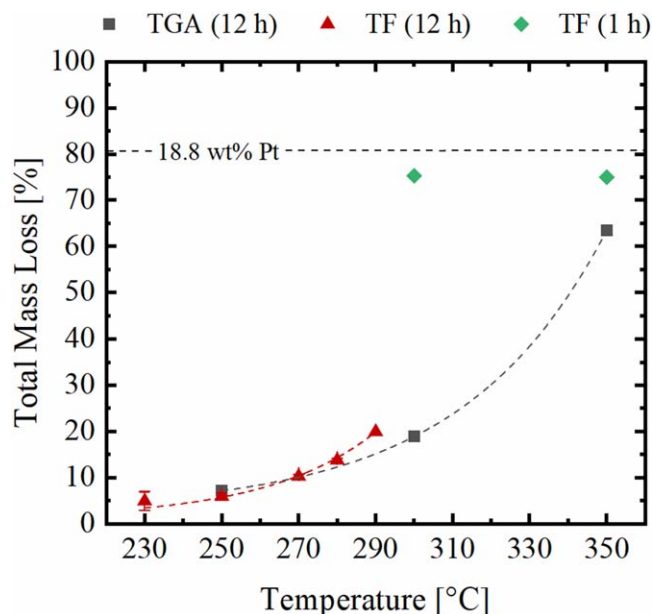


Figure 2. Total mass loss of the pristine Pt/KB catalyst under an air/argon mixture flow as a function of oxidation temperature measured after 12 h either for 10 mg pristine Pt/KB in the TGA (black squares) or for 300 mg pristine Pt/KB in the tube furnace (red triangles). Owing to the rapid mass loss in the tube furnace at ≥ 300 °C, the mass loss is reported after only 1 h of oxidation (green diamonds). The dashed lines serve as a guide to the eye, for exact values see Table I.

Table I. Total mass losses upon 12 h of oxidation of the pristine Pt/KB catalyst in the tube furnace under an air/Ar mixture flow (1000/200 nccm) at various temperatures (Δm_{air}). This is compared to the mass loss observed up to the respective temperature under Ar flow (Δm_{Ar} ; from the data in Fig. 1) that is solely due to the loss of adsorbed water and functional groups. The difference between these two values is a zeroth-order estimate of the bulk carbon loss upon the oxidation treatment of the Pt/KB catalyst.

Temperature	Δm_{air} (%)	Δm_{Ar} (%)	Bulk C loss (%)
230 °C	5.1 ± 0.6	4.8	~0.3
250 °C	5.9 ± 0.8	5.3	~0.6
270 °C	10.3 ± 0.4	5.6	~4.7
280 °C	13.8 ± 0.4	5.8	~8.0
290 °C	19.9	5.9	~14

–independent oxygen transport resistances, limiting current measurements were also conducted at 170, 270, 350 and 500 kPa_{abs,inlet}.

Start-up/shut-down measurements with 50 cm² active area cells.—Initial H₂/air polarization curves were recorded after conditioning and then repeated after each 5 SUSD cycles. All polarization curves were taken in current-controlled mode identical to the procedure described for cells with an active area of 5 cm².

The SUSD cycling protocol was adopted from a previous publication of our group, which provides a detailed account of experimental setup and gas flow protocol.¹⁹ Briefly, sharp H₂/air fronts traveling through the anode compartment were generated by pneumatic valves switching between two humidified streams of H₂ and air. Both gas streams are controlled to maintain the same temperature, pressure, and relative humidity. A switch from air to H₂ simulates the start-up of a fuel cell, whereas the reverse switch, replacing air with H₂, results in a shut-down event. One SUSD cycle is thus defined as a shut-down event followed by a start-up event. All SUSD cycles were run at a temperature of 80 °C, 100% RH, and a

cell pressure of 150 kPa_{abs,inlet}. The H₂ and air flows at the anode were set to 75 nccm (on a dry gas basis), while the cathode air flow was kept at 100 nccm. Using equation 20 from Mittermeier et al.,¹⁹ this corresponds to a H₂/air front residence time of $\tau = 1.2$ s passing through the anode, calculated from the anode flow field channel volume ($V_{\text{FF}} = 1.24$ cm³), the compressed GDL void volume ($V_{\text{GDL}} = 0.56$ cm³), and an absolute volumetric flow rate of 87 cm³ min⁻¹ (on a wet gas basis) at 80 °C, 150 kPa_{abs,inlet}, and 100% RH. The time between each start-up and shut-down event was 120 s.

Results and Discussion

Characterization of structural changes during localized oxidation.—The first objective of this work is to assess the relationship between increasing degrees of localized carbon oxidation and structural changes to the catalyst morphology. To this end, commercially available Pt/Ketjenblack (Pt/KB) is heated to target temperatures between 230 °C and 290 °C and oxidized for 12 h under an air/Ar mixture flow. While non-catalyzed carbon supports are mostly unreactive towards oxygen below 500 °C, Stevens et al. have observed carbon loss in the presence of Pt nanoparticles and air at temperatures as low as 150 °C and identified Pt-catalyzed carbon oxidation to CO₂ as the main pathway.²³ Since the catalytic oxidation reaction is kinetically controlled, the degree of localized carbon oxidation over a given time period is solely a function of the oxidation temperature. The resulting catalysts are labeled as such throughout this work, e.g., Pt/KB-230 °C for a catalyst kept at 230 °C for 12 h.

Figure 2 displays the temperature-dependent total mass loss of pristine Pt/KB determined *via* thermogravimetric analysis (10 mg sample; black squares) and scaled-up tube furnace experiments (300 mg sample; red triangles). Between 230 °C–290 °C, the mass losses after 12 h obtained from both methods agree quite well, with the total catalyst mass loss ranging between 5 and 20 wt%. These quantities, however, do not directly translate to a bulk carbon loss from the carbon support as CO₂. Instead, one has to take into account the desorption of moisture adsorbed in pores and on Pt particle surfaces as well as the loss of functional groups attached to the carbon surface (primarily carboxyl groups decomposing as CO₂).²⁴ We approximate the mass of bulk carbon loss due to Pt-catalyzed oxidation by comparing the total catalyst mass losses upon oxidation under the air/argon mixture flow (Δm_{air}) with values obtained in pure argon at the same temperature (Δm_{Ar}), based on the data shown in Fig. 1. While thermal treatment in argon readily removes moisture and labile functional groups up to 300 °C, it should not be capable of oxidizing the bulk carbon material itself. Thus, the difference in mass loss (i.e., $\Delta m_{\text{air}} - \Delta m_{\text{Ar}}$) is an approximate measure of the amount of bulk carbon loss; the latter is shown in the last column of Table I and increases from ~0.3 to ~14 wt% as the oxidation temperature increases from 230 to 290 °C. Upon increasing the tube furnace temperature to 300 °C and beyond, we observe an essentially complete oxidative carbon loss after only 1 h in the tube furnace (green diamonds), contrary to the substantially lower carbon mass loss observed in the TGA experiments with a temperature-hold time of 12 h (gray squares). This unexpected rapid transition from a gradual increase of the carbon mass loss with temperature to its complete oxidation at ≥ 300 °C in the tube furnace is likely a result of heat transfer limitations in the experimental setup: The exothermal formation of CO₂ (-393 kJ mol⁻¹)²⁵ generates heat locally within the catalyst powder that is contained by an alumina crucible placed in the tube furnace, and the heat generation rate upon carbon oxidation apparently exceeds the heat transfer rate from the surface of the catalyst powder in the crucible to the gas passing by above the crucible, resulting in a thermal runaway event. In our setup, 300 °C constitutes this tipping point, limiting the temperature range in this study to 290 °C (better heat transfer and thus higher controllable oxidation temperatures would be expected for a plug-flow or fluidized bed configuration). We thus note that while reaction temperature and duration can in principle be used to

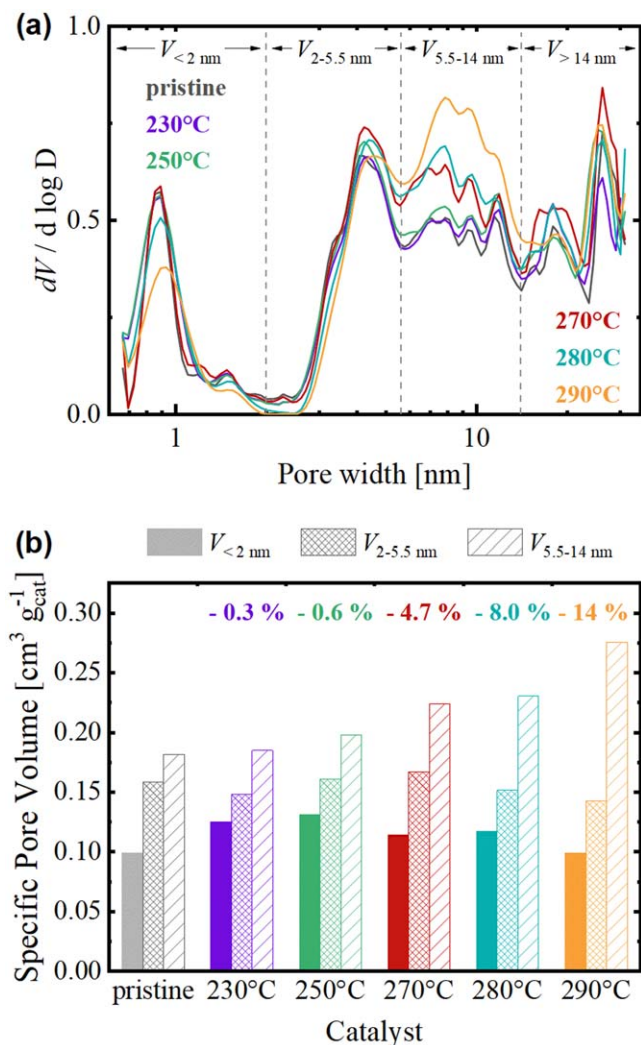


Figure 3. (a) Differential pore size distribution determined by N_2 physisorption for the pristine Pt/KB catalyst and for the catalysts oxidized in the tube furnace at various temperatures for 12 h. The vertical dashed lines indicate the pore width boundaries used for segmentation of the volumina contained in different pore size ranges. (b) Resulting specific micro- and mesopore volumes as segmented in (a), with the numbers placed above the bars marking the estimated bulk carbon loss (see Table I). For exact specific pore volume values see Table II.

control the degree of carbon oxidation of the Pt/KB catalyst, heat transfer constraints for a given setup must be considered. On account of the much smaller sample mass, no such thermal runaway has been observed in the TGA experiments.

The effect of localized oxidation on the carbon support's pore morphology is characterized by N_2 physisorption. Figure 3 provides differential pore size distributions and pore volumes for the pristine Pt/KB catalyst and for those oxidized at the marked temperatures in the tube furnace for 12 h (i.e., the catalysts marked by the red triangles in Fig. 2), evaluated using a QSDFT kernel for slit/cylindrical carbon pores. The corresponding numerical values are given in Table II. As previously explored in the publications by General Motors,^{13,16} it is instructive to classify pores in carbon supports owing to their capability of hosting Pt nanoparticles, e.g., micropores narrower than 2 nm, Pt-hosting mesopores between 2–8 nm (or 4–7 nm) and even wider, mostly interparticle macropores. Here, we segment the pore size ranges in a slightly different manner, selecting pore size regions that are marked by the local minima in the pore size distribution shown in Fig. 3a. This will allow

a later correlation between changes in pore morphology and catalyst performance. In essence, we distinguish between micropores ($V_{<2 \text{ nm}}$), narrow mesopores ($V_{2-5.5 \text{ nm}}$), wide mesopores ($V_{5.5-14 \text{ nm}}$), and macropores ($V_{>14 \text{ nm}}$), which are marked by the vertical dashed lines in Fig. 3a.

Figure 3b then shows the specific pore volumes in the micropore, narrow, and wide mesopore range segments for pristine and oxidized catalysts. Omitted in Fig. 3b is the specific pore volume in the macropore segment, which largely captures interparticle phenomena between aggregates. This pore range is unlikely to exert significant influence on high current density performance because of the minor contribution of electrode through-plane diffusion to the total oxygen transport resistance.^{26,27} Comparing the specific pore volumes between the pristine Pt/KB catalyst and those catalysts oxidized at 230 and 250 °C, the overall increase in specific pore volume is driven mostly by increasing micropore volumes with oxidation temperature (see gray, purple, and green bars). At higher oxidation temperatures, the micropore volumes continuously decline. The narrow mesopore volume remains remarkably constant at all temperatures (see cross-hatched bars). In contrast, wide mesopores (hatched bars) are most severely affected by localized oxidation with the specific pore volumes increasing by almost 50% for an oxidation temperature of 290 °C. Notably, the largest volume gain in the specific volume of the wide mesopores occurs at temperatures of 270 °C and above, coinciding with the onset of substantial bulk carbon loss (Table I). The process creating wide mesopores thus seems to be the main driver of oxidative carbon removal. Despite the more drastic evolution of wide mesopores at high oxidation temperatures, the total specific pore volumes of Pt/KB-280 °C and -290 °C decline marginally relative to the maximum attained for Pt/KB-270 °C. We ascribe this to a simultaneously occurring carbon oxidation process driven by the minor fraction of externally deposited Pt nanoparticles. Without pore containment, this oxidation proceeds indiscriminately on the external carbon surface and does not contribute to pore formation. As this effectively increases the weight fraction of platinum, the total specific pore volume (in cm³ per gram of catalyst) may decrease, even if carbon porosity increases. Normalized to the carbon mass, the total specific pore volume remains practically constant for oxidation temperatures of 270 °C (0.92 cm³ g⁻¹C), 280 °C (0.91 cm³ g⁻¹C), and 290 °C (0.93 cm³ g⁻¹C), suggesting an increased extent of external, non-contributing carbon oxidation. This is presumably because carbon oxidation rates accelerate more rapidly than rates of oxygen pore diffusion, shifting towards external carbon loss at higher temperatures.

In short, the morphological impact of localized oxidation manifests itself in two distinct pore types, (a) an initial increase in microporosity (< 2 nm) at low temperatures up to 250 °C with very small bulk carbon mass losses (see Table I), and (b) an opening of wide mesopores with diameters of 5.5–14 nm at 270 °C and above, concomitant with substantial bulk carbon losses. These pore types bear certain resemblance to the recently reported tomographic reconstructions of PtCo/Ketjenblack and modifications thereof, whereby no disclosure was made how the modified carbon supports (or catalysts) were prepared.¹⁷ In the work of these authors, the primary carbon particles are shown to possess slit-shaped micropores (1–2 nm width), connecting the outer surface area to internal mesopores, which give the primary particles a hollow morphology. For unmodified Ketjenblack, the internal mesopores range from 3–10 nm (7 nm average), increasing to 7–14 nm after the modification of the carbon support (11 nm average). Their pore types mirror the trends that we observe here for the micropores with <2 nm ($V_{<2 \text{ nm}}$ range in Fig. 3a) and the wide mesopores ($V_{5.5-14 \text{ nm}}$ range in Fig. 3a), respectively, for which we observe the most significant changes with increasing degrees of localized carbon oxidation. The fact that changes to the micro- and mesopore region appear at distinctly different oxidation temperatures should permit a clear correlation of these pore size changes to the electrochemical performance of the respective catalysts.

Table II. Numerical evaluation of the nitrogen physisorption data shown in Fig. 3 for the pristine Pt/KB catalyst and for Pt/KB oxidized in the tube furnace at various temperatures for 12 h. The specific surface area is calculated using the BET model (S_{BET}) as well as using a QSDFT kernel for slit/cylindrical carbon pores applied to the adsorption branch (S_{DFT}), showing good agreement. The same kernel is used to calculate total pore volume (V_{DFT}) and the pore volume in each of the pore size range segments that are outlined in Fig. 3a.

Catalyst	S_{BET}	S_{DFT}	V_{DFT}	$V_{< 2 \text{ nm}}$	$V_{2-5.5 \text{ nm}}$	$V_{5.5-14 \text{ nm}}$	$V_{> 14 \text{ nm}}$
	(m ² g ⁻¹)				(cm ³ g ⁻¹)		
Pt/KB	553	516	0.63	0.10	0.16	0.18	0.19
Pt/KB-230 °C	603	592	0.66	0.13	0.15	0.19	0.20
Pt/KB-250 °C	637	613	0.69	0.14	0.16	0.20	0.20
Pt/KB-270 °C	620	602	0.74	0.11	0.17	0.22	0.24
Pt/KB-280 °C	603	588	0.72	0.12	0.15	0.23	0.22
Pt/KB-290 °C	565	547	0.72	0.10	0.14	0.28	0.20

Oxygen reduction reaction kinetics in H₂/O₂.—In order to quantify the impact localized oxidation exerts on the oxygen reduction reaction (ORR) kinetics, we characterized pristine and oxidized catalysts electrochemically in single-cell measurements using 5 cm² MEAs. Low cathode Pt loadings of the pristine and oxidized Pt/KB within a narrow range of $0.062 \pm 0.004 \text{ mg}_{\text{Pt}} \text{ cm}^{-2}$ were prepared in order to keep the influence of loading variability on ORR kinetics below 3 mV (assuming a theoretical Tafel slope of 70 mV dec⁻¹; see Table III for details). Anode loadings were substantially higher ($0.10 \text{ mg}_{\text{Pt}} \text{ cm}^{-2}$) to exclude interferences originating from the anodic hydrogen oxidation reaction. First, we evaluated changes to the catalyst's electrochemically active surface area (ECSA) extracted from the H_{UPD} region. Increasing oxidation temperatures result in a monotonically decreasing ECSA, which is approximately 20% lower for the catalyst oxidized at 290 °C for 12 h than for the pristine catalyst. Notably, the relationship between oxidation temperature and ECSA loss is roughly linear (see Table III). This suggests that the ECSA loss is caused by Pt nanoparticle sintering rather than by Pt particle detachment and coalescence that would be caused by the loss of bulk carbon, as in the latter case the ECSA loss should follow the accelerating bulk carbon loss with temperature (see Table I).

Next, we turn to the effect of localized oxidation on the H₂/O₂ performance. Uncorrected differential flow polarization curves in H₂/O₂ at 80 °C, 100% RH, and 170 kPa_{abs, inlet} for all catalysts are presented in Fig. 4a together with the corresponding high frequency resistance (R_{HFR}) values. While the cell voltages at low current densities (e.g., 0.2 A cm^{-2}) decrease slightly with increasing oxidation temperature, consistent with the decrease of the ECSA (see Table III), all oxidized catalysts outperform the pristine Pt/KB by 15–25 mV at 2 A cm^{-2} . The origin of this substantial improvement

of the high-current density performance despite the loss of ECSA is somewhat unexpected: the H₂/O₂ performance should not be affected by oxygen transport resistances on account of the absence of an inert diluent (N₂) and of the high oxygen partial pressure, so that the morphological changes to the carbon support pore structure should play no role under these conditions. However, a second possible transport limitation that could be affected by the carbon support morphology and surface properties is the proton conduction resistance, both across the electrode and locally in the vicinity of the carbon primary particles and the Pt nanoparticles. The former is captured by the through-plane proton conduction resistance of the cathode electrode ($R_{\text{H}^+, \text{cath}}$), which we determine from electrochemical impedance spectroscopy (EIS) via a transmission line model. Values for all catalysts at 70% and 100% RH are shown in Figs. 4b and 4c, respectively, where it is apparent that $R_{\text{H}^+, \text{cath}}$ decreases from the value obtained for electrodes with pristine Pt/KB to between 15% for Pt/KB-230 °C and 40% for Pt/KB-290 °C. It should be noted that these changes in $R_{\text{H}^+, \text{cath}}$ with changing carbon morphology are much smaller than that reported by Ramaswamy et al. for carbon supports with similarly varying pore size distributions.¹⁶ Prior to examining the contribution of this non-negligible decrease in $R_{\text{H}^+, \text{cath}}$ to the H₂/O₂ performance difference at 2 A cm^{-2} , we will first examine whether the differences in $R_{\text{H}^+, \text{cath}}$ are indeed due to a catalyst induced change in the through-plane proton resistivity ($\rho_{\text{H}^+, \text{cath}}$) of the electrodes. The latter is obtained by dividing $R_{\text{H}^+, \text{cath}}$ by the cathode electrode thickness determined for each cathode electrode from SEM micrographs of MEA cross-sections (see Appendix). The thus determined $\rho_{\text{H}^+, \text{cath}}$ values at 70% and 100% RH are shown for the pristine and the oxidized Pt/KB-based electrodes in Figs. 4d and 4e, whereby the $\rho_{\text{H}^+, \text{cath}}$ values for each material are derived from two separate

Table III. Cathode Pt loadings (L_{Pt}), mean thickness (t_{CL}), and electrochemical properties for the cathodes with pristine Pt/KB catalyst and with Pt/KB oxidized in the tube furnace at various temperatures for 12 h, as well as with a pristine Pt/Vu catalyst. The electrochemically active surface areas (ECSA) were obtained from the H_{UPD} region in cyclic voltammetry. The ORR mass activity (i_{m}) determined at $0.9 \text{ V}_{\text{IR-free}}$ at the experimentally used conditions (80 °C, 100% RH, H₂/O₂ (2000/5000 nccm), 170 kPa_{abs}) and the Tafel slope (TS) were extracted from H₂/O₂ polarization curves after correcting for the high frequency resistance (R_{HFR}), the effective proton conduction resistance in the catalyst layer ($R_{\text{H}^+, \text{cath}}^{\text{eff}}$), the H₂ crossover, and the shorting current (the thus corrected data are shown in Fig. 5). The mass activity (i_{m}^*) was also extrapolated to the common reference condition of 103 kPa_{abs} O₂ (equivalent to 150 kPa_{abs} at 100% RH) according to the procedure described in the text; the specific activity (i_{s}^*) was then determined by dividing i_{m}^* and the ECSA for each electrode. The given values represent the mean of two independently prepared and measured MEAs and the indicated variation mark the min/max values, except for t_{CL} , where it represents the standard deviation of electrode thickness variation as described in the Appendix.

Catalyst	L_{Pt} ($\mu\text{g}_{\text{Pt}} \text{ cm}^{-2}$)	t_{CL} (μm)	ECSA (m ² _{Pt} g ⁻¹ _{Pt})	i_{m} (A g ⁻¹ _{Pt})	i_{m}^* (A g ⁻¹ _{Pt})	i_{s}^* ($\mu\text{A cm}^{-2}$ _{Pt})	TS (mV dec ⁻¹)
Pt/KB	61 ± 2	7.4 ± 0.4	78 ± 1	349 ± 16	280 ± 13	360 ± 19	89 ± 1
Pt/KB-230 °C	62 ± 2	6.6 ± 0.5	75 ± 1	345 ± 3	277 ± 3	369 ± 7	81 ± 0
Pt/KB-250 °C	64 ± 1	7.3 ± 0.7	73 ± 2	283 ± 36	227 ± 29	310 ± 30	75 ± 4
Pt/KB-270 °C	61 ± 3	6.4 ± 0.5	68 ± 1	278 ± 32	223 ± 26	329 ± 42	76 ± 2
Pt/KB-280 °C	64 ± 1	5.0 ± 0.5	66 ± 1	234 ± 7	188 ± 6	285 ± 8	78 ± 1
Pt/KB-290 °C	63 ± 3	5.2 ± 0.4	61 ± 1	207 ± 17	165 ± 13	269 ± 17	78 ± 1
Pt/Vu	69 ± 1	—	61 ± 1	118 ± 2	94 ± 2	154 ± 1	77 ± 0

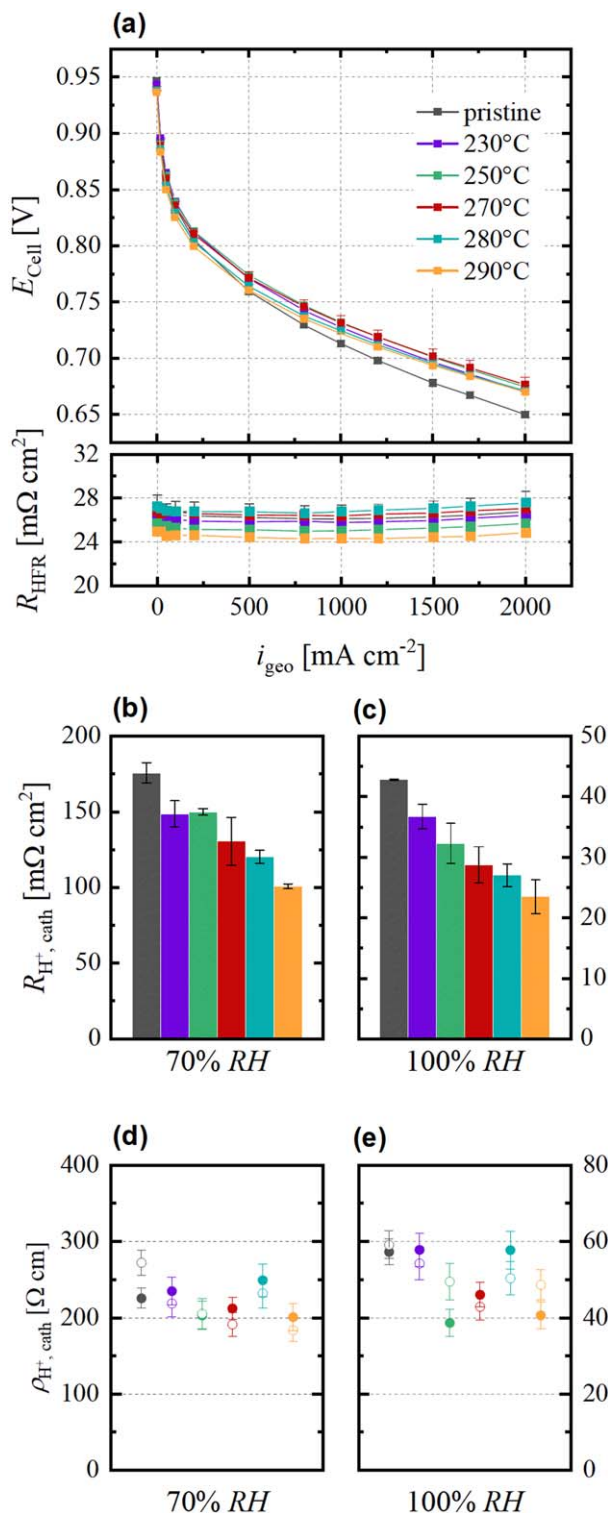


Figure 4. (a) Uncorrected H_2/O_2 polarization curves (80 °C, 100% RH, H_2/O_2 (2000 nccm/5000 nccm), 170 kPa_{abs,inlet}) and corresponding high frequency resistance (R_{HFR}) for the pristine Pt/KB catalyst and for the catalysts oxidized in the tube furnace at various temperatures for 12 h, with cathode platinum loadings of $0.062 \pm 0.004 \text{ mg}_{\text{Pt}} \text{ cm}^{-2}_{\text{geo}}$ (see Table III) and anode loadings of $0.100 \pm 0.015 \text{ mg}_{\text{Pt}} \text{ cm}^{-2}_{\text{geo}}$. (b) Cathode electrode through-plane proton conduction resistance ($R_{\text{H}^+, \text{cath}}$) determined from impedance spectroscopy at 70% RH and (c) at 100% RH. (d) Cathode electrode proton resistivity obtained by normalizing $R_{\text{H}^+, \text{cath}}$ to the catalyst layer thickness, given for two independent MEAs per catalyst, at 70% RH and (e) at 100% RH. Color coding in (b)–(e) identical to (a). The error bars in (a)–(c) represent the absolute deviation between independent measurements of two separate MEAs; the error bars in (d)–(e) are based on error propagation of the uncertainty introduced by the catalyst layer thickness variation.

MEAs, with error bars representing the uncertainty based on the cathode electrode thickness variation. In contrast to the quite clear continuous decrease of $R_{\text{H}^+, \text{cath}}$ with increasing oxidation temperature by up to 40% (Figs. 4b/4c), the decrease of $\rho_{\text{H}^+, \text{cath}}$ on the oxidation temperature is only up to 20% (Figs. 4d/4e), whereby this trend is rather weak due to the large experimental error on account of the electrode's thickness variation alone. Thus, a definitive statement on the effect of the oxidative treatment on the through-plane proton resistivity of the cathode electrode cannot be made. Furthermore, it should be noted that these measurements cannot provide any insights as to whether the oxidative treatment may possibly improve the local proton conductivity in the vicinity of the carbon primary particles and the Pt nanoparticles.

This leaves the question whether the decreasing values of $R_{\text{H}^+, \text{cath}}$ with increasing oxidation temperature (Figs. 4b/4c) are sufficient to explain the observed increase in the high-current density H_2/O_2 performance (Fig. 4a). For this, one needs to consider the current density-dependent cathode utilization, which is captured by the effective proton conduction resistance $R_{\text{H}^+, \text{cath}}^{\text{eff}} = R_{\text{H}^+, \text{cath}}^{\text{eff}} / (3 + \xi)$, where ξ is a correction factor that increases with current density (with $\xi = 0$ at $i = 0 \text{ A cm}^{-2}$).²⁸ Based on this, one can convert the H_2/O_2 performance data in Fig. 4a into an R_{HFR} - and $R_{\text{H}^+, \text{cath}}^{\text{eff}}$ -corrected Tafel plot vs the mass-normalized current density, which is corrected for the H_2 crossover ($5.5 \pm 0.5 \text{ mA cm}^{-2}$) and the shorting current. Now we can evaluate to what extent the observed 20–25 mV H_2/O_2 performance gain at 2 A cm^{-2} for the MEAs with the oxidized Pt/KB catalysts over those with the pristine Pt/KB catalyst (Fig. 4a) is related to the lower through-plane proton conduction resistance of the former (see Figs. 4b/4c): If the higher performance of the MEAs with the oxidized Pt/KB catalysts at 2 A cm^{-2} were indeed related solely to their slightly lower R_{HFR} (by at most $\sim 3 \text{ m}\Omega \text{ cm}^{-2}$, see lower panel in Fig. 4a) and their lower $R_{\text{H}^+, \text{cath}}$ (by 6–20 $\text{m}\Omega \text{ cm}^{-2}$, see Fig. 4d), their high current density performance in the resistance-corrected Tafel plot should become the same as that of the MEAs with the pristine Pt/KB catalyst. As shown in Fig. 5 this is not the case, with the resistance-corrected performance of the MEAs with the oxidized Pt/KB catalysts still being 9–20 mV higher at 2 A cm^{-2} , suggesting that additional effects must play a role.

From Fig. 5 we also determined the effective Tafel slope for a given cathode catalyst by linear fits through all points between 50 and $500 \text{ mA cm}^{-2}_{\text{geo}}$ (the lower limit is chosen to be 10 times larger than the H_2 crossover current to minimize its impact on fitting errors). It is evident from Fig. 5 that the Tafel slope of the MEAs with the pristine Pt/KB is substantially higher (89 mV dec^{-1} , see Table III) than that for the MEAs with the oxidized Pt/KB catalysts ($75\text{--}81 \text{ mV dec}^{-1}$, see Table III). However, even for the MEAs with the oxidized Pt/KB catalysts that yield the highest H_2/O_2 performance at 2 A cm^{-2} (Pt/KB-250 °C and Pt/KB-270 °C), the observed Tafel slopes of $75\text{--}76 \text{ mV dec}^{-1}$ still exceed the commonly assumed intrinsic value of 70 mV dec^{-1} that corresponds to a cathodic transfer coefficient of $\alpha_c = 1$ for the ORR.²⁹ Earlier work with MEAs that had the same I/C mass ratio (i.e., 0.65) with cathode catalysts where the Pt nanoparticles are located predominantly at the external surface of the carbon primary particles, namely either a Pt/Vu catalyst³⁰ (20 wt% Pt/Vu from TKK) or a catalyst based on the same KB support as used here for which Pt nanoparticles were deposited by a polyol-based method (referred to as Pt/KB_{P0} in Ref. 12), also yielded Tafel slopes of 76 mV dec^{-1} , i.e., much lower than the 89 mV dec^{-1} obtained for the pristine Pt/KB catalysts. On one hand, this suggests that the Pt nanoparticles of the oxidized Pt/KB catalysts are highly accessible, as is the case for catalysts where Pt particles are deposited predominantly on the exterior surfaces of the primary particles of the carbon support.

On the other hand, if we exclude oxygen transport losses, which are generally not observed with pure O_2 as a cathode gas, as an explanation for the superior high current density performance of the MEAs with the oxidized Pt/KB catalysts that is observed in the Tafel analysis of the H_2/O_2 data (Fig. 5), we are left with proton conduction limitations that are not captured by the through-plane

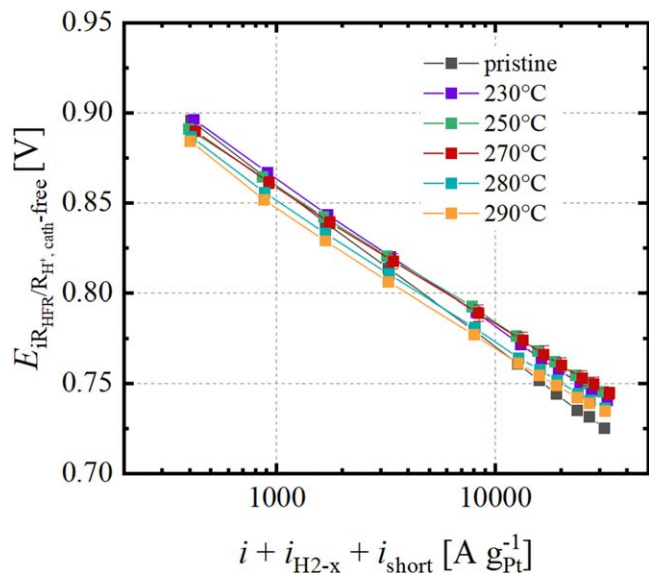


Figure 5. Tafel plot representation of the R_{HFR} - and $R_{\text{H}^+, \text{cath}}^{\text{eff}}$ -corrected H_2/O_2 cell voltage vs the Pt loading-normalized current density corrected for the H_2 crossover (i_{H_2-x}) and shorting current (i_{short}). The data are based on the differential flow H_2/O_2 polarization curves at 80 °C, 100% RH, 170 kPa_{abs,inlet} that are shown in Fig. 4a and the $R_{\text{H}^+, \text{cath}}$ values in Fig. 4c. Error bars represent the absolute deviation between independent measurements of two separate MEAs.

proton conduction resistance of the cathode electrodes. One may hypothesize that the oxidative treatment at elevated temperatures alters the surface hydrophobicity of the carbon pore surfaces, affecting their interaction with the ionomer film and with interfacial water. Ketjenblack is known to have hydrophilic surface groups

contributing to water sorption, and the mechanism and role of proton availability in ionomer-inaccessible micropores remains an ongoing matter of scientific debate.^{31,32}

In addition to Tafel slopes, we also determined the ORR mass activities for all catalysts from the linear fits in Fig. 5 by extrapolation to 0.9 V_{iR-free}; the values for all MEAs are summarized in Table III. As expected for a porous carbon support, Pt/KB can sustain a high mass activity of 349 A g⁻¹_{Pt}. In order to allow an easier comparison with the existing literature, we additionally converted the mass activity to the more commonly used reference conditions of 103 kPa O₂ and H₂ (equivalent to 150 kPa_{abs} O₂ and H₂ at 100% RH). For extrapolating the recorded ORR mass activity (i_m) to its value at this reference condition, denoted as i_m^* , a kinetic reaction order with respect to the oxygen partial pressure of $\gamma = 0.75$ was used (for a more detailed discussion, see the voltage loss analysis section). While Pt/KB-230 °C matches the activity of the pristine Pt/KB, further increases in oxidation temperature lower the mass activity by up to 40% (Pt/KB-290 °C). The sintering-induced loss of ECSA (discussed above) is a likely cause, but higher degrees of oxidation and concomitant pore opening might also increase ionomer poisoning and thus depress the catalyst's intrinsic kinetics. We distinguish between these effects by comparing the catalyst's specific activity, i_s^* (see Table III), which normalizes the converted mass activity (i_m^*) to the ECSA. The overall loss of specific activity is less stark at all oxidation temperatures, confirming that ECSA reduction *via* sintering is predominantly responsible for the lowered mass activity. Furthermore, specific activity losses exceed 15% only for the MEAs with the Pt/KB-280 °C and Pt/KB-290 °C catalysts, where N₂ physisorption measurements show the most severely widened pore structure. Increased ionomer intrusion and poisoning effects seem therefore to be restricted to highly oxidized carbon supports. In the context of the aforementioned tradeoff between solid and porous carbon supports, it is also interesting to compare the kinetics of oxidized catalysts to those of a reference catalyst on solid carbon (20 wt% Pt/Vulcan). Its mass activity of 118 A g⁻¹_{Pt} is ca. 3

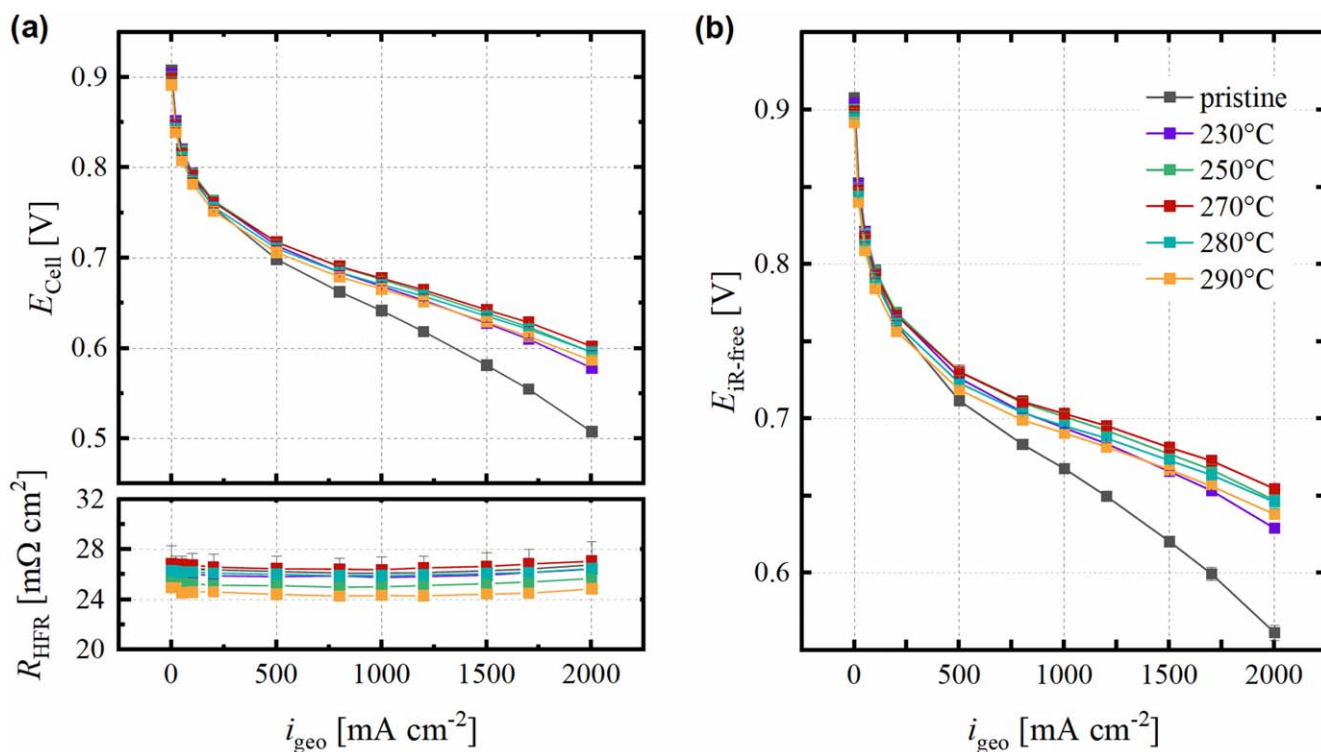


Figure 6. (a) Uncorrected H_2/air polarization curves (80 °C, 100% RH, H_2/Air (2000 nccm/5000 nccm), 170 kPa_{abs,inlet}) and corresponding R_{HFR} for the pristine Pt/KB catalyst and for the catalysts oxidized in the tube furnace at various temperatures for 12 h, with cathode platinum loadings of $0.062 \pm 0.004 \text{ mg}_{\text{Pt}} \text{ cm}^{-2}_{\text{geo}}$ (see Table III) and anode loadings of $0.100 \pm 0.015 \text{ mg}_{\text{Pt}} \text{ cm}^{-2}_{\text{geo}}$. Color coding identical to (b). (b) iR_{HFR} -corrected polarization curves. Error bars represent the absolute deviation between independent measurements of two separate MEAs.

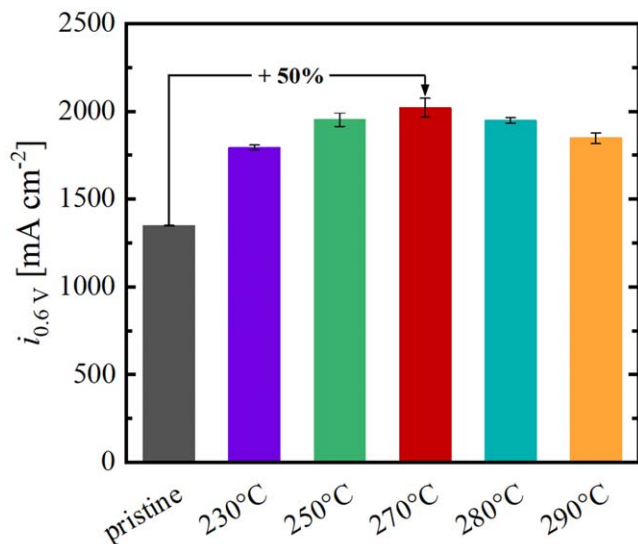


Figure 7. Current density reached during polarization in H_2/air (80 °C, 100% RH, differential flow, 170 kPa_{abs,inlet}) at an uncorrected cell voltage of 0.60 V for pristine and oxidized catalysts at $0.062 \pm 0.004 \text{ mg}_{\text{Pt}} \text{ cm}^{-2}_{\text{geo}}$ loading, based on the data shown in Fig. 6a. Error bars represent the absolute deviation between independent measurements of two different MEAs.

times lower than that for the pristine Pt/KB catalyst with a porous carbon support, in good agreement with literature-reported estimates of ionomer poisoning.¹¹ Due to the higher *ECSA* of the Pt/KB catalyst (78 vs 61 $\text{m}^2_{\text{Pt}} \text{ g}^{-1}_{\text{Pt}}$), the specific activity is a better comparison and yields $154 \mu\text{A cm}^{-2}_{\text{Pt}}$ for Pt/Vu, which is still ~ 2.5 times lower compared to the pristine Pt/KB. Crucially, this specific activity is still 40% lower than for the most severely oxidized catalyst, Pt/KB-290 °C ($i_s^* = 269 \mu\text{A cm}^{-2}_{\text{Pt}}$), demonstrating that even the highest degrees of localized oxidation attained in this study do not introduce comparable levels of ionomer poisoning seen on a typical solid carbon support with predominantly external Pt particles.

High current density performance in H_2/Air .—Polarization curves in H_2/O_2 allowed to quantify the effect of localized carbon oxidation on the intrinsic ORR kinetics and revealed a slightly improved high current density performance upon the oxidative treatment, albeit at the cost of *ECSA* loss and, to a lesser degree, increased ionomer poisoning with higher degrees of oxidation. Systematic increases in pore accessibility, however, should have the most profound effect on oxygen diffusion, which should become more apparent with air rather than oxygen feed. We demonstrate this in H_2/air polarization curves for pristine and oxidized catalysts, given in Fig. 6a. As expected, the low current density performance follows the trend of ORR mass activities observed in O_2 : The pristine Pt/KB performs well owing to its high *ECSA* and the extensive shielding of the Pt nanoparticles from ionomer poisoning. *ECSA* and the extent of ionomer shielding deteriorate progressively with higher oxidation temperatures, resulting in the lowest kinetic performance for the MEAs with the Pt/KB-290 °C catalyst.

At high current densities, the restricted pore accessibility in pristine Pt/KB impedes efficient oxygen diffusion to the internal Pt nanoparticles and the cell voltage drops rapidly with increasing current density. In contrast, catalysts that have undergone localized carbon oxidation show drastically superior high current density performance. Even at the lowest oxidation temperature (230 °C), the cell voltage at 2 A cm^{-2} increases by 70 mV compared to the pristine Pt/KB catalyst. The progression of high current density performance with further increasing oxidation temperatures is resolved more clearly in R_{HFR} -corrected polarization curves (Fig. 6b). In this case, the improvement of the Pt/KB-230 °C

catalyst over the pristine Pt/KB catalyst at 2 A cm^{-2} is 72 mV, while that of the Pt/KB-250 °C and the Pt/KB-270 °C catalysts increases even further to 86 mV and 93 mV, respectively. For the Pt/KB-280 °C and the Pt/KB-290 °C catalysts, this trend reverses and their high current density performance is inferior to that of the Pt/KB-270 °C catalyst (although still vastly outperforming the pristine Pt/KB catalyst by 85 mV and 77 mV, respectively). Localized carbon oxidation thus clearly reduces voltage losses in the oxygen transport-limited regime, confirming the successful conversion from a porous to an “accessible porous carbon” support morphology. Another way to illustrate the impact of localized carbon oxidation is to compare the current density achieved at a certain cell voltage. Due to vehicular heat rejection constraints, operating a fuel cell at voltages below 0.60–0.67 V is generally not feasible. Going to higher current densities is only sensible as long as the cell voltage remains sufficiently high. We therefore take the increase in current density attainable at 0.60 V as a measure of performance improvement after localized carbon oxidation. As can be seen from Fig. 7, the lowest degree of oxidation attained at 230 °C already results in an increase in current density from $\sim 1350 \text{ mA cm}^{-2}$ to $\sim 1800 \text{ mA cm}^{-2}$. The maximum improvement is achieved at 270 °C with $\sim 2020 \text{ mA cm}^{-2}$ at 0.6 V, translating to an increase of $\sim 50\%$ in power density.

Two central observations arise from this. First, catalyst performance at high current densities does not improve indefinitely with increasing degrees of oxidation. Instead, the decline in cell voltage at 2 A cm^{-2} beyond an oxidation treatment at 270 °C indicates the existence of an optimal degree of oxidation, suggesting that two counteracting effects on the cell performance are at play. Second, the largest incremental performance gain is conferred at the lowest oxidation temperatures, i.e., at conditions where the bulk carbon loss is below 5 wt% (see Table III); treatment at temperatures that yield higher bulk carbon loss yield diminishing high current density improvements over the pristine Pt/KB catalyst. The responsible mechanism enabling higher cell performance must therefore be active at comparatively minor changes to pore morphology and bulk carbon mass. We answer these questions in the following section with the aid of limiting current measurements.

The origin of improved high current density performance.—

The existence of a performance maximum for the Pt/KB-270 °C catalyst can be conceptualized as a Pareto-optimal degree of localized carbon oxidation. As such, higher and lower oxidation temperatures or, more precisely, higher and lower degrees of bulk carbon mass loss, both affect the catalyst properties negatively, resulting in lower high current density performance. Which parameters are traded off against each other in search of this optimum degree of oxidation? Analogous to the comparison of solid and porous carbon supports by Yarlagadda et al.,¹³ we posit a balance between ORR kinetics and oxygen transport. The relationship between kinetics and oxidation temperature has been investigated above, revealing a progressing loss of catalyst ORR mass activity with higher oxidation temperatures. This is primarily due to sintering-based particle growth, reducing the Pt *ECSA*, and secondarily exacerbated by increased exposure of Pt nanoparticles to the ionomer and a concomitant poisoning of the ORR activity.

The impact of localized oxidation on the oxygen transport properties can be quantified by limiting current measurements. Following the methodology established by Baker et al., the total oxygen transport resistance, $R_{\text{O}_2}^{\text{total}}$, can be separated into its pressure-dependent and pressure-independent contributions ($R_{\text{O}_2}^{\text{PD}}$ and $R_{\text{O}_2}^{\text{PI}}$, respectively).³³ As depicted in Fig. 8, $R_{\text{O}_2}^{\text{PD}}$ (solid columns) is constant for all catalysts at $0.40 \pm 0.02 \text{ s cm}^{-1}$. This is expected, because pressure dependencies in oxygen transport mainly arise from molecular diffusion in flow field channels and gas diffusion media, which were identical for all experiments. In contrast, $R_{\text{O}_2}^{\text{PI}}$ captures pressure-independent phenomena ascribed to Knudsen diffusion through carbon pores in the primary carbon

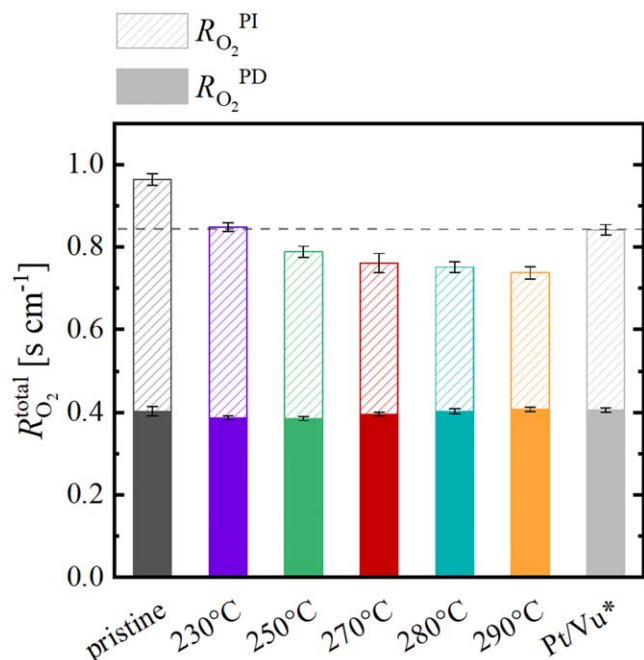


Figure 8. Total oxygen transport resistance for pristine and oxidized Pt/KB catalysts, segmented into pressure-dependent ($R_{O_2}^{PD}$, solid bars) and pressure-independent contributions ($R_{O_2}^{PI}$, hatched bars) that were determined from limiting current measurements with various O_2 concentrations at 80 °C, 70% RH, differential flow (2000/5000 nccm), and pressures of 170, 270, 350, and 500 kPa_{abs}. The dashed horizontal line indicates the total oxygen transport resistance for a catalyst supported on solid carbon with a comparable roughness factor (Pt/Vulcan, 0.07 mg_{Pt} cm⁻², $rf = 43$ cm²_{Pt} cm⁻²_{electrode}). Error bars represent the absolute deviation between independent measurements of two different MEAs.

particles, to oxygen diffusion through the ionomer film around the Pt nanoparticles, and to interfacial effects.^{34–36} As such, they are amenable to changes in carbon support morphology imparted by the process of localized carbon oxidation. This is indeed the case: the Pt/KB-230 °C catalyst exhibits a strongly reduced pressure-independent transport resistance of 0.46 ± 0.01 s cm⁻¹ (purple hatched bar in Fig. 8), compared to 0.56 ± 0.01 s cm⁻¹ for the Pt/KB catalyst (gray hatched bar). $R_{O_2}^{PI}$ decreases further to 0.36 ± 0.02 s cm⁻¹ for the catalyst oxidized at 270 °C, a ~40% reduction vs the pristine Pt/KB catalyst. Interestingly, the higher degrees of localized carbon oxidation achieved at 280 °C and 290 °C (see Table I) do not benefit oxygen transport, as $R_{O_2}^{PI}$ reaches a plateau within the accuracy of the measurement. Note that $R_{O_2}^{PI}$ for catalysts oxidized at 250 °C and above is even lower than that of Pt/Vu (light-gray hatched bar) with a comparable roughness factor ($rf = 43$ cm²_{Pt} cm⁻²_{electrode}, based on $L = 0.07$ mg_{Pt} cm⁻² and $ECSA = 62$ m² g⁻¹_{Pt}). This is somewhat surprising, as the majority of Pt nanoparticles for commercial Pt/Vu catalysts is reported to be located on the external surfaces (between 80%–100% according to Padgett et al.⁶ and Ito et al.⁷), so that one would expect only minor oxygen transport resistances through micro- and narrow mesopores for the Pt/Vu catalyst. The even lower $R_{O_2}^{PI}$ values for the Pt/KB catalysts oxidized between 250 °C–290 °C thus suggests a nearly complete absence of pore diffusion effects, and additionally an improved Pt/ionomer interface (i.e., reduced diffusion resistance through the ionomer film covering the catalyst surface).¹⁶

We can now examine in more detail the possible causes for the performance maximum observed for the Pt/KB-270 °C catalyst, considering both the dependence of the ORR kinetics and of the oxygen transport resistance on the extent of localized carbon oxidation. At oxidation temperatures up to 270 °C, the up to ~20% loss of ORR mass activity (see Table III) is overcompensated by outsized improvements in pore accessibility as reflected by the up

to ~35% lower $R_{O_2}^{PI}$ (see Fig. 8), strongly reducing the voltage loss at high current densities. At 280 and 290 °C, aggravated Pt nanoparticle sintering and ionomer poisoning lead to deteriorating ORR mass activity (by ~30% and ~40%, respectively), which is not anymore compensated by additional decreases in $R_{O_2}^{PI}$, so that the high current density performance decreases as a result (see Fig. 8). The degree of localized carbon oxidation attained at 270 °C, characterized by a bulk carbon mass loss of ~5 wt% is Pareto-efficient with respect to kinetics and pore accessibility.

The remaining question is which morphological changes of the carbon support are the most critical for the observed gains in pore accessibility and the concomitant reduction in $R_{O_2}^{PI}$. H₂/air polarization curves show the largest incremental improvement in high current density performance at the lowest oxidation temperature (230 °C) and, accordingly, limiting current measurements reveal the most significant decrease in $R_{O_2}^{PI}$. The changes in pore volume distributions evident at this temperature are rather minor, with the loss of bulk carbon remaining below 1 wt% (see Table I). Analysis of the pore size distribution correlates this carbon loss to an increase in $V_{<2\text{ nm}}$, which Ko et al. ascribe to slit-shaped micropores in the outer shell of primary carbon particles.¹⁷ Apparently, the increase/creation of these pores is primarily responsible for the increased oxygen diffusivity to internal Pt nanoparticles and enables the enormous increase in high current density performance. Similar observations are made for the changes in micropore volume and pressure-independent oxygen transport resistance at temperatures up to 270 °C, although the marginal decrease in $R_{O_2}^{PI}$ gets lower with each temperature increment. For 270 °C and beyond, the dominant change in pore structure is the volume increase in wide mesopores ($V_{5.5-14\text{ nm}}$) that is accompanied by substantial bulk carbon loss (≥ 5 wt%). Limiting current measurements for these catalysts, however, show no further reduction of $R_{O_2}^{PI}$, implying that the (excessive) generation of wide mesopores within the carbon support does not contribute to meaningful improvements in oxygen transport.

It may appear surprising at first that the minute bulk carbon losses observed after oxidation at 230 °C and 250 °C (<1 wt%, see Table I) result in such outsized improvements in oxygen transport, while major increases in the catalysts' mesoporosity are largely ineffective towards this end. However, if micropores in the outer carbon layers constitute the bottleneck for oxygen diffusivity to internal Pt particles, the initial loss of bulk carbon in the opening of such slit pores would indeed yield the greatest marginal benefit to $R_{O_2}^{PI}$. We therefore conclude that Pt accessibility and efficient oxygen transport is primarily achieved by opening up microporous constrictions in the outer carbon shell, which requires very low degrees of bulk carbon oxidation.

H₂/air performance voltage loss analysis.—Based on the measured ORR mass activities and all the transport resistances discussed in the previous sections, the various voltage loss terms and the resulting H₂/air polarization curves can be predicted for each catalyst. An agreement of the predicted polarization curve for a given ORR catalyst with the experimentally obtained polarization curve would then imply that all voltage losses have been accounted for, while a divergence would suggest that some contributions were not adequately captured. A detailed description of the following voltage loss analysis and its theoretical background can be found in earlier publications; here we only briefly summarize our approach and refer to the relevant equations by their enumeration in the original accounts.^{29,37,38} Initially, the equilibrium cell potential is calculated for the experimental cell temperature and pressure based on the Nernst equation, assuming full humidification, i.e., a water activity of unity (see Eq. 2 in Ref. 29). Note that the oxygen partial pressure in our experiments is affected by the pressure drop between cathode inlet and outlet ($p_{inlet} = 170$ kPa_{abs} and $p_{outlet} = 150$ kPa_{abs}) at the here used differential flows. Thus, an average cathode pressure of 160 kPa_{abs} was taken to calculate the oxygen partial pressure. From the purely thermodynamic H₂/air potential, we subsequently subtract the current density dependent voltage loss contributions

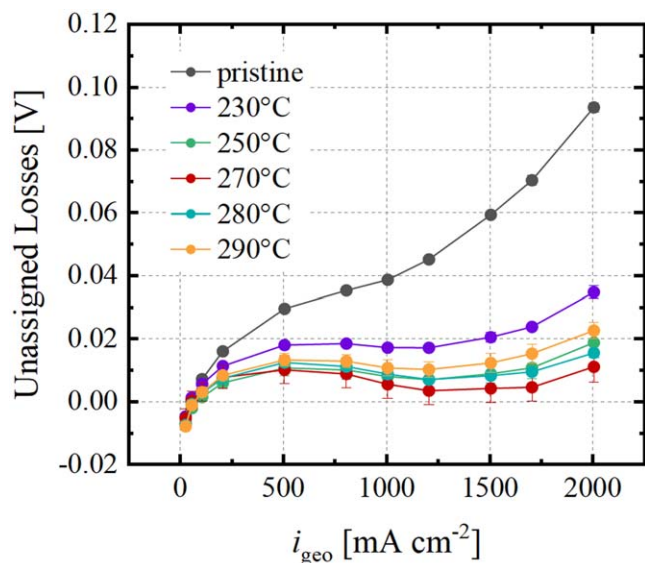


Figure 9. Unassigned voltage losses for the H_2/air polarization curves shown in Fig. 6a (80 °C, 100% RH, differential flow, 170 kPa_{abs,inlet}) for the pristine Pt/KB catalyst and for the catalysts oxidized in the tube furnace at various temperatures for 12 h. The unassigned voltage losses remain after correcting for the ORR overpotential (η_{ORR}), the high frequency resistance (R_{HFR}), the effective proton conduction resistance of the cathode catalyst layer ($R_{\text{H}^+, \text{cath}}^{\text{eff}}$), and the total oxygen transport resistance ($R_{\text{O}_2}^{\text{total}}$). Error bars represent the absolute deviation between independent measurements of two different MEAs.

from: (i) the ORR overpotential (η_{ORR} , based on the mass activities in Table I); (ii) the ohmic drop based on the measured high frequency resistance (R_{HFR} ; shown in Fig. 6a); (iii) the effective through-plane proton conduction resistance ($R_{\text{H}^+, \text{cath}}^{\text{eff}}$) that is calculated from the measured $R_{\text{H}^+, \text{cath}}$ values (see Fig. 4c); and, iv) the total oxygen transport resistance ($R_{\text{O}_2}^{\text{total}}$, shown in Fig. 8). The geometric current density is also corrected for the hydrogen crossover current and the shorting current using a mean value of 5 mA cm⁻² and the hydrogen oxidation overpotential (η_{HOR}) was considered negligible at the here used anode Pt loadings.³⁹

To quantify the ORR overpotential, we assumed simple Tafel kinetics with a frequently assumed single intrinsic Tafel slope of 70 mV dec⁻¹, corresponding to a cathodic transfer coefficient of $\alpha_c = 1$ (see eq. 3 in Ref. 29). Note that using the experimentally determined Tafel slopes (75–89 mV dec⁻¹) instead of the single intrinsic Tafel slope would overestimate the ORR overpotential, as the higher experimental values suggest that the intrinsic kinetics are masked by a remaining, still unaccounted-for transport resistance even in pure O₂ (see previous section on oxygen reduction reaction kinetics in H₂/O₂). The value of the exchange current density was obtained by extrapolating the ORR mass activity at 0.9 V_{ir-free}, 80 °C, and average O₂ and H₂ partial pressures of 160 kPa (i_m in Table III) to the reversible potential at these conditions using a Tafel slope of 70 mV dec⁻¹. To predict the ORR overpotential for a H₂/air polarization curve, however, the exchange current density needs to be scaled to the relevant lower oxygen partial pressure (see eq. 4 in Ref. 29). This dependency is described by γ , the kinetic reaction order of the ORR with respect to the oxygen partial pressure at constant ORR overpotential and constant H₂ partial pressure (not to be confused with the also frequently used reaction order m of the ORR with respect to p_{O_2} at constant $E_{\text{ir-free}}$ and constant p_{H_2} , whereby $m = \gamma + \alpha_c/4$ ³⁷). The originally reported value for γ was 0.54,²⁹ but later on values ranging from 0.6 to 0.75 have been reported.³⁷ Setting γ to the upper end of these values, i.e., to 0.75, gave the best agreement with the experimental H₂/air polarization curves at current densities below 100 mA cm⁻², where purely

kinetic effects are at play. Thus, γ is set to 0.75 throughout the entire voltage loss analysis. Next, ohmic losses can be calculated in a straightforward manner from the high frequency resistance (R_{HFR} , using the experimental values from Fig. 6a, averaged for each catalyst over the entire current density range), which combines the bulk proton conduction resistance of the membrane as well as the contact resistances between diffusion medium/catalyst layer and diffusion medium/flow fields. The voltage losses due to the effective through-plane proton conduction resistance in the cathode catalyst layer ($R_{\text{H}^+, \text{cath}}^{\text{eff}}$) are determined from the measured $R_{\text{H}^+, \text{cath}}$ values (see Fig. 4c), taking into account the current-density dependent correction factor for the cathode utilization as discussed in the previous section on ORR kinetics (see Eq. 20 in Ref. 28). Finally, the voltage losses related to the oxygen mass transport from the flow field channels to the Pt nanoparticles in the catalyst layer are considered. The effectively lower oxygen partial pressure at the catalyst surface increases η_{ORR} in analogy to the ORR kinetics discussed above, while simultaneously decreasing the reversible cell voltage according to the Nernst equation. Both effects are captured using the total oxygen transport resistance determined from limiting currents ($R_{\text{O}_2}^{\text{total}}$, taken from Fig. 8) and taking $\alpha_c = 1$ and $\gamma = 0.75$ (see Eq. A11 in Ref. 38).

On this basis, we can now compare the H₂/air polarization curves predicted on the basis of the measured ORR kinetics and transport resistances for all catalysts with their observed H₂/air performance. Figure 9 shows the unassigned losses, i.e., the difference between the predicted and the observed cell voltage as a function of current density. In all cases, the unassigned losses are largest at high current densities, reflecting the importance of correctly capturing transport losses. The MEAs with the pristine Pt/KB catalyst (gray symbols) already show substantial unassigned losses at low current densities, which is explained by the difference between the assumed intrinsic Tafel slope (70 mV dec⁻¹) used for the predicted polarization curve and the experimentally determined value from the H₂/O₂ performance (89 mV dec⁻¹, see Fig. 5 and Table III). For the oxidized Pt/KB catalysts, the measured Tafel slopes are closer to the expected value and the unassigned losses in the kinetic region are lower in turn. The most significant difference in unassigned losses, however, is observed at high current densities, where they range between 11 mV (Pt/KB-270 °C) and 94 mV (Pt/KB) at 2 A cm⁻². This evident decrease of unassigned losses with improved carbon support pore accessibility strongly suggests that the limiting current method underestimates the oxygen transport resistance in pristine Pt/KB, while the transport within oxidized catalysts is captured more accurately. We hypothesize that this discrepancy is rooted in the determination of the oxygen transport resistance by limiting current experiments: In a H₂/air polarization curve (e.g., at 2 A cm⁻² and 0.5–0.6 V), internal Pt nanoparticles are still reached by oxygen and thus ORR-active, but experience oxygen transport resistances due to pore diffusion. On the other hand, under limiting current conditions (4–5 A cm⁻² and 0.05–0.3 V), the smaller fraction of external Pt nanoparticles should consume all the oxygen before it enters the internal pores due to their extremely high ORR activity. The measured oxygen transport resistance then would mainly capture diffusion to the externally accessible Pt nanoparticles rather than the additional oxygen transport resistance within the carbon pores. When the oxidative opening of microporous bottlenecks increases accessibility of inner Pt nanoparticles, polarization curves and limiting current measurements come into better agreement. In short, localized carbon oxidation of Pt/KB catalysts not only substantially improves their high current density performance, but also leads to a more accurate assessment of voltage loss contributions, particularly with respect to oxygen mass transport. As a consequence, the unassigned voltage loss observed for pristine Pt/KB catalysts essentially disappear for the most active Pt/KB-270 °C catalyst, suggesting that pore diffusion effects constitute a major part of the unassigned losses. Similar conclusions were drawn by Ramaswamy

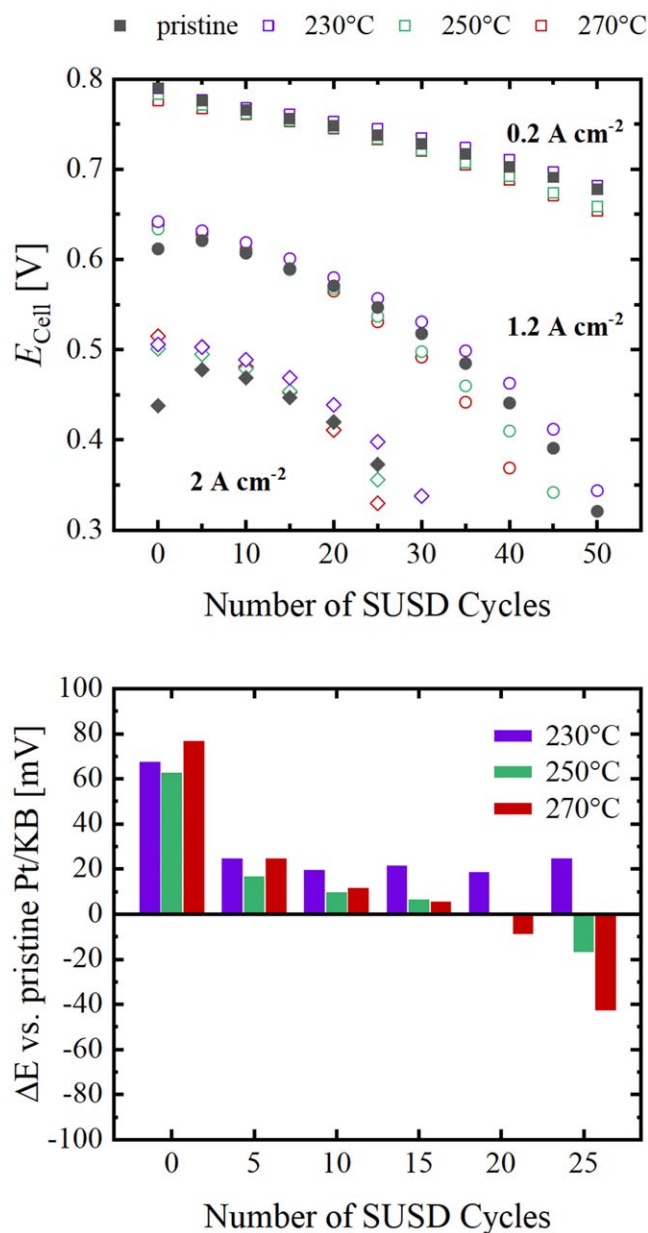


Figure 10. (a) Evolution of the cell voltage at select current densities (extracted from H₂/air polarization curves in a 50 cm² single-cell) as a function of SUSD cycles (1 start-up and 1 shut-down) for the pristine Pt/KB catalyst (gray) and for the catalysts oxidized at 230 °C (purple), 250 °C (green), and 270 °C (red). The anode and cathode Pt loadings are $0.100 \pm 0.015 \text{ mg}_{\text{Pt}} \text{ cm}^{-2}_{\text{geo}}$ and $0.100 \pm 0.004 \text{ mg}_{\text{Pt}} \text{ cm}^{-2}_{\text{geo}}$, respectively. (b) Cell voltage difference at 2 A cm⁻² for locally oxidized catalysts relative to the pristine Pt/KB as a function of SUSD cycle number. SUSD conditions: 80 °C, 100% RH, 150 kPa_{abs,inlet}, 75 nccm H₂/air anode flow, 100 nccm air cathode flow corresponding to an anode H₂/air front residence time of $\tau = 1.2 \text{ s}$. H₂/air polarization curve conditions: 80 °C, 100% RH, 170 kPa_{abs,inlet} and 2000 nccm H₂/5000 nccm air on anode and cathode, respectively.

et al., who were able to predict voltage losses more accurately when using catalysts supported on Vulcan carbon (MSC-a) rather than on high surface area carbons.¹⁶

Start-Up/shut-down degradation.—We have shown that the localized carbon oxidation of Pt/KB clearly enables high current density operation at much higher cell voltages, but it remains to be determined whether the intentional bulk carbon mass loss induced by such an oxidative pre-treatment leads to a greater susceptibility towards SUSD degradation. During SUSD cycles, transient H₂/air

fronts in the anode compartment lead to oxygen reduction in the air-filled parts of the anodic catalyst layer, which must be matched by an oxidative current at the adjacent cathode electrode segment. This can only happen *via* the oxidation of water through the oxygen evolution reaction (OER) on the cathode catalyst or, more importantly, *via* the electrochemical oxidation of the carbon of the cathode catalyst support. Once the amount of carbon lost due to SUSD-induced carbon oxidation exceeds a certain threshold, the carbon structure collapses under the compressive force applied to the MEA (commonly referred to as “cathode thinning”). This sudden loss of electrode void volume severely limits oxygen diffusion and voltage losses due to mass transport quickly reach hundreds of millivolts. Earlier work found such structural collapse to typically occur at carbon losses around 10 wt%,⁴⁰ begging the question of whether locally oxidized Pt/KB catalysts with similar bulk carbon losses (e. g., ~5 wt% for the highest performing Pt/KB-270 °C catalyst, see Table I) face accelerated collapse as well.

We simulate SUSD cycles at 80 °C and 100% RH in a 50 cm² active area single-cell by pneumatic valve-controlled switching of the anode gas feed between separately humidified streams of H₂ and air. This generates sharp H₂/air fronts with an approximate residence time of $\tau = 1.2 \text{ s}$ (see Experimental section and Ref. 19 for details). Note that these conditions are much more severe than expected for realistic SUSD events, which typically occur outside the driving operation when the fuel cell stack is at ambient temperature and humidifiers are not operating. The accelerated protocol used here is designed to maximize observable differences in catalyst SUSD durability. After every five cycles, another H₂/air polarization curve is recorded to quantify the voltage losses induced by SUSD degradation. The cell voltages obtained at 0.2 A cm⁻² (kinetic regime), 1.2 A cm⁻² (intermediate regime) and 2 A cm⁻² (mass transport-limited regime) are extracted and plotted as a function of the SUSD cycle number to compare the SUSD-induced voltage losses in Pt/KB, Pt/KB-230 °C, Pt/KB-250 °C and Pt/KB-270 °C (Fig. 10a).

Comparing the initial H₂/air polarization curves to the initial performance of 5 cm² MEAs with the same catalyst shown above, it is evident that the cell voltages obtained at 0.2 A cm⁻² in the 50 cm² cell are approximately 20 mV higher. This is expected and reflects the faster ORR kinetics due to the higher cathode loading ($0.10 \text{ vs } \sim 0.06 \text{ mg}_{\text{Pt}} \text{ cm}^{-2}$). At 1.2 and 2 A cm⁻², this observation reverses and the 50 cm² cell performance across all catalysts is lower by 20 and by 60–80 mV, respectively. The increasing divergence with higher current densities clearly points to more severe mass transport limitations compared to the 5 cm² cell. We ascribe this to two causes: First, supply limitations required a switch to a different gas diffusion medium that unfortunately displayed a higher R_{HFR} ($32 \text{ vs } 25 \text{ m}\Omega \text{ cm}^2$) and also somewhat higher oxygen transport resistances. Second, a cerium-mitigated membrane was used to exclude premature membrane degradation from the SUSD protocol. MEAs based on this membrane, however, suffer an increasing performance loss at high current densities ($>1 \text{ A cm}^{-2}$) that increases with current density, which we ascribe to the effect of current density driven Ce³⁺ migration to the cathode electrode’s ionomer phase and the associated concentration polarization (described for other cations in Ref. 41). Both effects most severely depress cell voltages at high current densities and thus contribute to the lower high current density performance observed with the 50 cm² cell measurements. At the same time, these lower absolute cell voltages at high current densities that are caused by differences in the membrane and the diffusion media are not expected to affect the SUSD degradation rates. Therefore, the 50 cm² based SUSD data shown in the following should yield a reliable comparison of the SUSD degradation rates between the pristine Pt/KB catalyst and the Pt/KB catalysts oxidized at various temperatures.

At the lowest current density of 0.2 A cm⁻², the cell voltages decrease linearly over the first ~20 SUSD cycles for all catalysts (see upper set of lines in Fig. 10a). As cell voltages in the kinetic regime are effectively a function of the available Pt surface area, this

agrees well with the similar rate of cycling-induced ECSA loss observed in all catalysts. A different trend is observed at 1.2 and 2 A cm⁻², where mass transport limitations play a dominant role and where the regime of linear degradation rates extends only over a shorter number of SUSD cycles (a well-known characteristic of SUSD degradation^{19,40}): Pt/KB-230 °C maintains higher cell voltages compared to the pristine Pt/KB, demonstrating both higher performance and greater stability towards SUSD degradation. In contrast, Pt/KB-250 °C and Pt/KB-270 °C initially outperform Pt/KB, but display higher rates of SUSD degradation proportional to their oxidation temperatures, i.e., a more rapid loss of cell voltage and accelerated structural collapse of the electrode. This becomes evident at 1.2 A cm⁻² after ~20 SUSD cycles and at 2 A cm⁻² after ~10 SUSD cycles, indicating that the loss of bulk carbon during the oxidative pre-treatment in fact increases SUSD susceptibility. However, in the application-relevant regime, i.e., over the number of SUSD cycles where the SUSD related performance loss at high current densities is <50 mV (i.e., over the first 10 cycles in this strongly accelerated SUSD test at 80 °C and with long H₂/air front residence times), the differences in SUSD degradation rates between the Pt/KB-230 °C catalyst (~0.3 wt% bulk carbon loss, see Table I) and the Pt/KB-270 °C catalyst (~5 wt% bulk carbon loss) with the highest beginning-of-life performance (see Fig. 7) are rather minor.

A highly interesting observation can be made from the cell voltage changes of pristine Pt/KB at 2 A cm⁻² (gray symbols in Fig. 10a): in contrast to all locally oxidized catalysts, the cell voltage increases by 50 mV after five SUSD cycles compared to the initial polarization curve. Clearly, the electrochemical carbon corrosion suffered in the first five SUSD cycles leads to a performance improvement that seems to resemble the effect of thermal localized carbon oxidation. Due to the oxidative nature of both reactions, it is highly likely that a similar mechanism is at play, removing carbon from pores which act as a bottleneck for oxygen transport towards internal Pt particles. A similar performance increase upon the initial electrochemical oxidation of the catalyst carbon support was observed previously (see Fig. 5 in Ref. 42), but could not be explained at that time.

Although we find modestly accelerated SUSD degradation for oxidation temperatures of 250 °C and beyond, this does not outweigh the performance benefits conferred by localized oxidation. For all catalysts, the difference in cell voltage at 2 A cm⁻² (ΔE) vs the pristine Pt/KB as a function of SUSD cycle number is shown in Fig. 10b. Pt/KB-230 °C consistently achieves higher cell voltages than the pristine catalyst for the whole degradation protocol, even though the difference reduces to 20–30 mV after the performance gain of Pt/KB in the first five SUSD cycles. Thus, a mild degree of localized oxidation leads to both superior performance and SUSD resilience compared to the pristine catalyst. Pt/KB-250 °C and Pt/KB-270 °C, with higher carbon loss during localized oxidation (see Table I), lose their initial performance advantage over Pt/KB after 15–20 SUSD cycles. Their cell voltages then drop rapidly below the value achieved by the pristine catalyst. At this level of SUSD degradation, however, all catalysts have already suffered voltage losses of 50–100 mV compared to their initial performance, which would constitute end-of-life for any practical application. In short, while higher degrees of localized oxidation lead to accelerated SUSD degradation, this durability penalty should be inconsequential and does not limit the practical applicability of catalysts pretreated with this method.

Conclusions

In this work, we have systematically investigated the localized oxidation of commercial Pt/KB, a pre-treatment well-suited to increase the accessibility of Pt nanoparticles located inside porous carbon supports, lowering the pressure-independent oxygen transport resistance. Platinum nanoparticles hosted within carbon pores catalyze the oxidative removal of bulk carbon in their vicinity, thereby increasing pore width and volume within the support.

Analysis of the pore size distribution revealed two distinct changes to the pore morphology, with oxidation temperatures below 270 °C primarily increasing the micropore volume (at a bulk carbon mass loss of <1 wt%), whereas oxidation temperatures between 270 °C–290 °C predominantly generate wide mesopores accompanied by substantial bulk carbon loss (up to 14 wt%).

Following structural characterization, H₂/air polarization curves using locally oxidized catalysts in low-loaded cathodes (0.06 mg_{Pt} cm⁻²) demonstrated significant improvements in high current density performance to the tune of 70–90 mV at 2 A cm⁻² compared to the pristine catalyst. Considering 0.6 V as a lower bound for cell operation on account of heat rejection constraints, this is equivalent to a 50% increase in current density at this cell potential. Importantly, the largest marginal voltage gain was observed already at the lowest oxidation temperature of 230 °C (70 mV at 2 A cm⁻²), where the catalyst exhibited increases predominantly in the micropore volume. In conjunction with limiting current measurements, a strongly decreased pressure-independent oxygen transport resistance was found, suggesting that the opening of constricting micropores is responsible for better oxygen diffusion to internal Pt particles. We also observed a performance maximum at 270 °C and a subsequent trend reversal at higher oxidation temperatures. This is explained as a trade-off between ORR mass activity, which is increasingly lost due to Pt sintering and ionomer poisoning, and pore accessibility, encountering diminishing returns to further pore widening at higher degrees of oxidation. Conceptually, the degree of oxidation in Pt/KB-270 °C is Pareto-optimal with respect to ORR kinetics and oxygen mass transport.

Lastly, we investigated the susceptibility of locally oxidized catalysts towards SUSD degradation, prompted by the hypothesis that thermal carbon oxidation during the pre-treatment might accelerate the collapse of the electrode structure, similar to electrochemical carbon corrosion in SUSD. Although we found increased SUSD susceptibility for Pt/KB catalysts oxidized at 250 °C and 270 °C, their accelerated degradation exceeded voltage losses of the commercial catalyst only after the high current density performance of all materials had decreased by 50–100 mV vs their initial performance. This cross-over point would be well within end-of-life for any practical application, making the slightly increased susceptibility inconsequential. On the other hand, while the Pt/KB catalyst oxidized at 230 °C had a 15–20 mV lower beginning-of-life H₂/air performance than those oxidized at 250 °C and 270 °C, it still offered a 70 mV performance benefit over the pristine Pt/KB and exhibited a lower SUSD degradation rate compared to the latter over the entire SUSD test sequence. This suggests that the performance gains produced by localized carbon oxidation need to be critically compared to the associated SUSD degradation rates, so that the optimally balanced catalyst might be the one oxidized at 230 °C.

Acknowledgments

We gratefully acknowledge funding from the Swiss National Foundation under the funding scheme Sinergia (project grant number 180335). We also express our gratitude to Ana Marija Damjanović for her help with the start-up/shut-down protocol and to Mohammad Fathi Tovini for valuable discussions of thermogravimetric analysis results. We further thank Katia Rodewald for her SEM micrographs of MEA cross-sections.

Appendix

The proton conduction resistivity of a catalyst layer ($\rho_{H^+, \text{cath}}$) is calculated by dividing the through-plane proton conduction resistance ($R_{H^+, \text{cath}}$) by the catalyst layer thickness (t_{CL}). Since the uncertainty of $\rho_{H^+, \text{cath}}$ is strongly affected by the variation in electrode thickness, both the mean value and the statistical distribution of t_{CL} are required. To this end, SEM micrographs of ion-milled MEA cross-sections fixated on a Cu tape are taken, with image acquisitions at 3–5 different locations for each MEA. An exemplary micrograph at a magnification of 2000x with the cathode catalyst

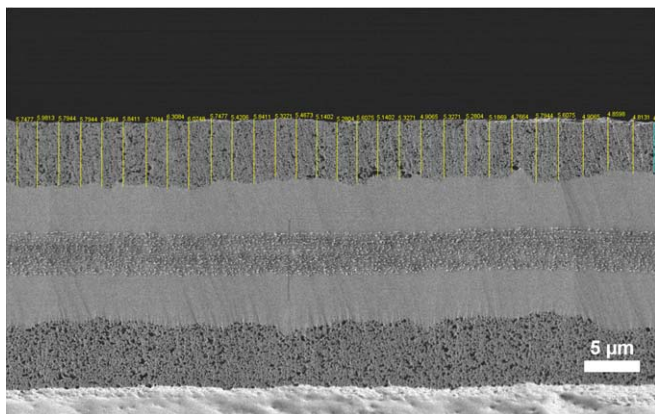


Figure A-1. Representative SEM micrograph of an ion-milled MEA cross section (2000x magnification). Thickness measurements of the cathode catalyst layer (top) are taken every $\sim 1.5 \mu\text{m}$ across the cross-sectional area to statistically evaluate the cathode thickness distribution along the MEA.

layer on top is shown in Fig. A-1. To get a statistically representative estimate of the cathode layer thickness, > 50 line measurements were taken at a lateral distance of approximately $1.5 \mu\text{m}$ across the entire polished area (yellow lines in Fig. A-1). Generally, the maximum variation in thickness is around $\pm 1 \mu\text{m}$. For each catalyst, the mean value of t_{CL} was calculated from all line measurements (given in Table III) and the corresponding standard deviation was taken as the uncertainty of t_{CL} for error propagation considerations.

ORCID

Timon Lazaridis  <https://orcid.org/0000-0003-3022-9140>
Hubert A. Gasteiger  <https://orcid.org/0000-0001-8199-8703>

References

- D. A. Cullen, K. C. Neyerlin, R. K. Ahluwalia, R. Mukundan, K. L. More, R. L. Borup, A. Z. Weber, D. J. Myers, and A. Kusoglu, *Nat. Energy*, **6**, 462 (2021).
- M. K. Debe, *Nature*, **486**, 43 (2012).
- C. S. Gittleman, A. Kongkanand, D. Masten, and W. Gu, *Curr. Opin. Electrochem.*, **18**, 81 (2019).
- A. Kongkanand and M. F. Mathias, *J. Phys. Chem. Lett.*, **7**, 1127 (2016).
- O. Gröger, H. A. Gasteiger, and J.-P. Suchsland, *J. Electrochem. Soc.*, **162**, A2605 (2015).
- E. Padgett et al., *J. Electrochem. Soc.*, **165**, F173 (2018).
- T. Ito, U. Matsuaki, Y. Otsuka, M. Hatta, K. Hayakawa, K. Matsutani, T. Tada, and H. Jinnai, *Electrochemistry*, **79**, 374 (2011).
- Y.-C. Park, H. Tokiwa, K. Kakinuma, M. Watanabe, and M. Uchida, *J. Power Sources*, **315**, 179 (2016).
- R. Subbaraman, D. Strmcnik, V. Stamenkovic, and N. M. Markovic, *J. Phys. Chem. C*, **114**, 8414 (2010).
- K. Shinozaki, Y. Morimoto, B. S. Pivovar, and S. S. Kocha, *J. Power Sources*, **325**, 745 (2016).
- T. Takeshita, Y. Kamitaka, K. Shinozaki, K. Kodama, and Y. Morimoto, *J. Electroanal. Chem.*, **871**, 114250 (2020).
- G. S. Harzer, A. Orfanidi, H. El-Sayed, P. Madkikar, and H. A. Gasteiger, *J. Electrochem. Soc.*, **165**, F770 (2018).
- V. Yarlagadda, M. K. Carpenter, T. E. Moylan, R. S. Kukreja, R. Koestner, W. Gu, L. Thompson, and A. Kongkanand, *ACS Energy Lett.*, **3**, 618 (2018).
- M. K. Carpenter and A. Kongkanand, "US patent application US."2017/0033368A1, filed July 31, 2015 and published Feb. 2, 2017.
- A. Kongkanand and M. K. Carpenter, "US patent application US."9,947,935B1, filed Sep. 30, 2016 and published Apr. 17, 2018.
- N. Ramaswamy, W. Gu, J. M. Ziegelbauer, and S. Kumaraguru, *J. Electrochem. Soc.*, **167**, 064515 (2020).
- M. Ko, E. Padgett, V. Yarlagadda, A. Kongkanand, and D. A. Muller, *J. Electrochem. Soc.*, **168**, 024512 (2021).
- C. A. Reiser, L. Bregoli, T. W. Patterson, J. S. Yi, J. D. Yang, M. L. Perry, and T. D. Jarvi, *Electrochem. Solid-State Lett.*, **8**, A273 (2005).
- T. Mittermeier, A. Weiß, F. Hasché, G. Hübner, and H. A. Gasteiger, *J. Electrochem. Soc.*, **164**, F127 (2017).
- T. Mittermeier, A. Weiß, F. Hasché, and H. A. Gasteiger, *J. Electrochem. Soc.*, **165**, F1349 (2018).
- C. Weidenthaler, *Nanoscale*, **3**, 792 (2011).
- T. R. Johns, R. S. Goeke, V. Ashbacher, P. C. Thüne, J. W. Niemantsverdriet, B. Kiefer, C. H. Kim, M. P. Balogh, and A. K. Datye, *J. Catal.*, **328**, 151 (2015).
- D. A. Stevens and J. R. Dahn, *Carbon*, **43**, 179 (2005).
- J. Jaramillo, P. M. Alvarez, and V. Gomez-Serrano, *Appl. Surf. Sci.*, **256**, 5232 (2010).
- E. J. Prosen and F. D. Rossini, *J. Res. Natl. Inst. Stand. Technol.*, **33**, 439 (1944).
- C. Wang, X. Cheng, J. Lu, S. Shen, X. Yan, J. Yin, G. Wei, and J. Zhang, *J. Phys. Chem. Lett.*, **8**, 5848 (2017).
- T. Schuler, A. Chowdhury, A. T. Freiberg, B. Sneed, F. B. Spingler, M. C. Tucker, K. L. More, C. J. Radke, and A. Z. Weber, *J. Electrochem. Soc.*, **166**, F3020 (2019).
- K. C. Neyerlin, W. Gu, J. Jorne, A. Clark, and H. A. Gasteiger, *J. Electrochem. Soc.*, **154**, B279 (2007).
- K. C. Neyerlin, W. Gu, J. Jorne, and H. A. Gasteiger, *J. Electrochem. Soc.*, **153**, A1955 (2006).
- A. Orfanidi, P. Madkikar, H. A. El-Sayed, G. S. Harzer, T. Kratky, and H. A. Gasteiger, *J. Electrochem. Soc.*, **164**, F418 (2017).
- T. Soboleva, K. Malek, Z. Xie, T. Navessin, and S. Holdcroft, *ACS Appl. Mater. Interfaces*, **3**, 1827 (2011).
- A. Chowdhury, R. M. Darling, C. J. Radke, and A. Z. Weber, *ECS Trans.*, **92**, 247 (2019).
- D. R. Baker, D. A. Caulk, K. C. Neyerlin, and M. W. Murphy, *J. Electrochem. Soc.*, **156**, B991 (2009).
- T. A. Greszler, D. Caulk, and P. Sinha, *J. Electrochem. Soc.*, **159**, F831 (2012).
- H. Liu, W. K. Epting, and S. Litster, *Langmuir*, **31**, 9853 (2015).
- H. Iden, T. Mashio, and A. Ohma, *J. Electroanal. Chem.*, **708**, 87 (2013).
- H. A. Gasteiger, W. Gu, R. Makharia, M. F. Mathias, and B. Sompalli, *Handbook of Fuel Cells*, ed. W. Vielstich et al. (Wiley, Chichester, UK) p. 593 (2010).
- P. Zihrl, I. Hartung, S. Kirsch, G. Huebner, F. Hasché, and H. A. Gasteiger, *J. Electrochem. Soc.*, **163**, F492 (2016).
- J. Durst, C. Simon, F. Hasché, and H. A. Gasteiger, *J. Electrochem. Soc.*, **162**, F190 (2015).
- P. T. Yu, W. Gu, R. Makharia, F. T. Wagner, and H. A. Gasteiger, *ECS Trans.*, **3**, 797 (2006).
- T. A. Greszler, T. E. Moylan, and H. A. Gasteiger, *Handbook of Fuel Cells*, ed. W. Vielstich et al. (Wiley, Chichester, UK) p. 728 (2010).
- H. A. Gasteiger, W. Gu, B. Litteer, R. Makharia, B. Brady, M. Budinski, E. Thompson, F. T. Wagner, S. G. Yan, and P. T. Yu, *Mini-Micro Fuel Cells*, ed. S. Kakac et al. (Springer, Dordrecht, NL) p. 225 (2008).